Available online at www.CivileJournal.org

Civil Engineering Journal

(E-ISSN: 2476-3055; ISSN: 2676-6957)

Vol. 12, No. 06, June, 2026

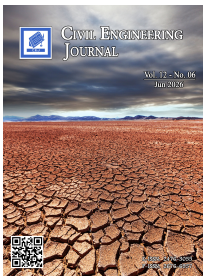

Tunnel-Induced Settlement: Analytical Validation and Parametric Study of Faulted Ground Under Rainfall Conditions

Zaid S. Alajlan [1], Loujain Suliman [2*], Hamzah M. B. Al-Hashemi [3], Ali Alatify [1]

[1] *Department of Civil Engineering, College of Engineering in Al-Kharj, Prince Sattam Bin Abdulaziz University, Al-Kharj,11942, Saudi Arabia.*

[2] *State Key Laboratory of Coal Mine Disaster Dynamics and Control, China Chongqing University, Chongqing 400044, China.*

[3] *Indian Institute of Technology Bombay, Powai, Mumbai 400076, Maharashtra, India.*

Received 22 March 2026; Revised 26 May 2026; Accepted 28 May 2026; Published 01 June 2026

Abstract

The increasing demand for underground infrastructure in densely populated urban areas has intensified the need for reliable prediction of tunneling-induced ground settlement, particularly under complex geological conditions such as fault zones. This study aims to investigate the effect of fault material properties and heavy rainfall on surface settlement induced by tunnel excavation. A coupled analytical and numerical approach was adopted to evaluate the ground response under faulted conditions. Finite element analysis was conducted to simulate tunnel excavation and ground deformation, while the proposed analytical solution was developed to predict settlement behavior. In addition, a parametric study was performed to investigate the influence of fault material characteristics under rainfall conditions on surface deformation. The obtained results indicate that fault zones significantly affect settlement magnitude and distribution, especially under heavy rainfall due to the reduction in shear strength and changes in hydro-mechanical behavior. The comparison between the analytical solution and numerical simulation demonstrates good agreement, confirming the validity and reliability of the proposed approach. The novelty of this study lies in integrating fault material properties and rainfall effects into the settlement prediction framework, providing a more comprehensive understanding of tunneling performance in faulted ground conditions and offering practical guidance for underground construction in complex urban environments.

Keywords: Rainfall; Faulted Ground; Pore Water Pressure; Settlement; Slope.

1. Introduction

As urban infrastructure expands rapidly, there is an increasing demand for underground space utilization; therefore, tunneling is one of the most important geotechnical activities. It causes surface settlement that can damage overlying infrastructure and utilities, and the excavation of the tunnel will create new stresses. Urban geotechnical engineering requires accurate prediction of tunnel-induced ground deformation. The early theoretical framework proposed by Peck (1969) [1] established the Gaussian distribution as a useful representation of the transverse settlement trough, and this continues to underpin a broad base of later studies. As tunnels become more complex in increasingly difficult geological conditions, there is a need for more advanced and validated predictive tools to capture the totality of the influencing factors on ground response.

Analytical solutions have long been favored in tunnel engineering practice for their computational efficiency and physically transparent formulations. Sagaseta (1987) [2] introduced a source-sink approach to estimate ground

* Corresponding author: lojain-s@hotmail.com

https://doi.org/10.28991/CEJ-2026-012-06-015

movements due to ground loss, providing closed-form expressions for displacement in incompressible soils. Building on this, Verruijt & Booker (1998) [3] extended the elastic solution to account for both uniform convergence and tunnel ovalization, enabling a more realistic representation of tunnel deformation mechanisms. Loganathan & Poulos (1998) [4] further refined the analytical framework by incorporating a modified ground loss parameter that accounts for the gap between the tunnel lining and surrounding ground, significantly improving settlement predictions. More recently, Guo et al. [5] proposed an optimized gap parameter theory combined with three-dimensional finite element analysis to investigate shield tunnel construction-induced ground settlement. Their study demonstrated that grouting filling ratio has the most significant impact on ground settlement, while tunnel face pressure and strata conditions also contribute meaningfully findings that reinforce the importance of construction-phase variables in settlement prediction beyond the classical gap formulation. Despite these advances, the foundational limitation of assuming homogeneous, isotropic ground conditions persists across most analytical methods, and none of these solutions accounts for geological discontinuities such as faults or for transient hydraulic effects induced by rainfall infiltration.

Rainfall infiltration constitutes a critical hydro-mechanical trigger for ground instability in tunneling, particularly in mountainous terrain with complex geology. Sustained rainfall raises the groundwater table, increases pore water pressure, and reduces the effective stress and shear strength of surrounding materials, thereby compromising the stability of both the excavation and the completed tunnel structure [6, 7]. Statistical analyses of documented incidents confirm that rainfall is the most frequently cited triggering factor in tunnel entrance collapse events, causing great casualties and economic losses in tunneling projects [8–11]. The tunnel entrance section of the construction collapsed which is allegedly due to weak stratum stability, poor construction, and sustained rainfall [12–14]. Among these contributing factors, rainfall stands out as a particularly critical trigger, with the majority of recorded tunnel entrance section collapse incidents being directly attributed to rainfall events [15, 16]. Consequently, investigating the precursory characteristics prior to rainfall-induced collapse at tunnel entrances under complex geological conditions is of considerable importance for effective prevention and remediation [17–20].

Li et al. [21] and Luo et al. [22] further demonstrated that construction-induced disturbance in loess tunnels produces significantly more pronounced and sudden settlement compared to conventional rock tunnels, highlighting the particular vulnerability of weaker formations to coupled excavation-hydraulic loading. Rainfall-driven recharge of high-pressure dissolution cavities has additionally been identified as a potential trigger for sudden water inrushes during excavation, exposing the completed tunnel lining to elevated water pressure [23, 24]. Concurrently, localized muddy limestone formations in close proximity to the lining become progressively water-saturated as a result of groundwater infiltration recharged by rainfall. This saturation process weakens the surrounding strata, leading to a measurable reduction in the bearing capacity of the tunnel lining [25-30]. In the broader geotechnical context, Bustamante et al. [31] recently conducted a sensitivity analysis of slope stability under heavy rainfall using PLAXIS 2D, the same software platform adopted in the present study, demonstrating that increasing rainfall duration progressively reduces matric suction, lowers shear strength, and decreases the factor of safety, with well-graded soils exhibiting up to 73.7% reduction in stability after 24 hours of sustained high-intensity rainfall. These findings collectively reinforce the critical importance of incorporating rainfall-induced pore water pressure evolution in any realistic assessment of tunnel-induced ground deformation, particularly in geologically faulted environments.

Geological faults represent one of the most challenging conditions encountered in tunnel construction, as they introduce zones of weakened, deformable material that disrupt the continuity of the surrounding rock mass and significantly alter the stress redistribution pattern around the tunnel. Numerical simulations and model tests have been applied extensively to study the mechanical behaviors and failure characteristics of tunnels under fault conditions. Yao et al. [26] applied numerical and experimental methods to examine the mechanical behavior and failure characteristics of tunnels under reverse fault conditions, revealing that fault geometry and material properties critically govern the extent of induced deformation. Kaya et al. [27] employed the finite element method to analyze the failure mechanism of a tunnel portal during excavation, identifying insufficient initial support and weathered rock masses as primary contributors to instability, and confirming that a rock retaining wall with jet grout columns is effective as a repair measure. Duan et al. [28] examined the impact of rainfall conditions on the stability of tunnel exit slopes through GeoStudio numerical simulations, concluding that rainfall scenarios produce the most unfavorable stability conditions. More recently, Zhang et al. [29] systematically varied fault zone core width, total zone width, dip angle, and dip direction through numerical simulation, establishing that reducing the fault core width intensifies the mechanical response of the tunnel lining due to stress concentration, while decreasing the dip angle transitions axial stress from tensile-compressive to predominantly compressive and increases relative deformation intensity. Furthermore, Wu et al. [30] investigated multi-line TBM tunneling through fractured zones using combined physical model testing, three-dimensional numerical simulation, and field monitoring, demonstrating that settlement peaks at the center of fractured zones and diminishes laterally, with amplified differential settlement in overlying buildings. Their findings also confirmed that crown grouting is the most effective deformation-mitigation strategy in fractured geological settings a conclusion that directly supports the grouting evaluation conducted in the present study. Collectively, these studies highlight the necessity of explicitly incorporating fault zone properties into both numerical and analytical modeling frameworks when tunneling in geologically complex terrain.

Despite significant progress in both analytical and numerical methods, a critical gap remains in literature. Existing analytical solutions, including the most recently optimized gap parameter framework of Guo et al. [5], are fundamentally restricted to homogeneous ground conditions and cannot capture the differential deformation behavior introduced by fault zones of varying mechanical properties. Even the most recent studies representing the current state of the art in fault-tunnel interaction, such as Zhang et al. [29] and Wu et al. [30], address fault geometry effects on lining stress and surface settlement in isolation, without coupling fault zone deformability with rainfall-driven pore water pressure changes. Similarly, Bustamante et al. [31] and Ma et al. [32] treat rainfall infiltration effects and grouting mitigation independently, without integrating them into a unified settlement prediction framework applicable to faulted ground. Consequently, compared with previous analytical solutions, the proposed method provides a more integrated framework for evaluating tunnel-induced settlement in complex geological conditions. Classical analytical approaches, such as those based on elastic cavity theory, are useful for rapid estimation of ground deformation, but they commonly assume homogeneous and isotropic ground conditions and therefore cannot fully represent the influence of geological discontinuities. Similarly, many numerical studies have investigated tunnel behavior under faulted or fractured ground conditions, but they often focus on stress redistribution, lining response, or settlement patterns without integrating rainfall-induced pore water pressure and mitigation measures within the same framework. The present study differs from these approaches by combining analytical settlement prediction with finite element validation, rainfall infiltration modeling, fault-property parametric analysis, and grouting evaluation. This integration improves the practical value of the method because it not only predicts settlement but also identifies the dominant controlling factors, particularly fault stiffness, fault multiplicity, and hydraulic boundary conditions. Therefore, the proposed framework provides a more comprehensive and design-oriented tool for preliminary assessment, risk evaluation, and reinforcement planning in tunnels constructed through faulted ground under rainfall conditions.

To address these gaps, the present study systematically investigates tunnel-induced settlement through the integration of analytical solutions and numerical modeling techniques. The analytical framework decomposes tunnel deformation into uniform radial convergence and tunnel ovalization components, which are superimposed to yield the total displacement field. Validation is performed through direct comparison with finite element numerical simulations conducted in PLAXIS 2D, using coupled hydro-mechanical models that incorporate rainfall infiltration as a transient flux boundary condition. Following validation, a comprehensive parametric study is conducted to evaluate the influence of rock faults under conditions of intensive rainfall infiltration, considering variations in fault material properties, specifically elastic modulus, cohesion, and friction angle, as well as fault quantity and orientation. The study further evaluates grouting as a mitigation measure by comparing the mechanical response of grouted and ungrouted fault scenarios. The outcomes of this study aim to provide a reliable, computationally efficient analytical tool for predicting tunnel-induced settlement in faulted ground under rainfall conditions, contributing a practical framework for preliminary design and risk assessment in complex geotechnical environments.

2. Methodology

2.1. The Simulation FEM

The Finite Element Method (FEM) is a widely used numerical technique for solving complex engineering problems involving continuum mechanics, particularly in geotechnical engineering. It works by discretizing a continuous domain into smaller elements, allowing the governing differential equations to be solved approximately over each element. This approach enables the analysis of stress–strain behavior, deformation, seepage, and coupled hydro-mechanical processes in soils and structures under various loading conditions. PLAXIS 2D is a specialized finite element software developed for the analysis of two-dimensional geotechnical problems. It is widely applied in modeling soil–structure interaction, slope stability, tunneling, excavation, and foundation behavior. PLAXIS 2D incorporates advanced constitutive models, such as the Mohr–Coulomb and Hardening Soil models, enabling realistic simulation of soil behavior under different stress paths. The software also supports coupled analyses, including groundwater flow and consolidation, making it particularly suitable for studying problems involving rainfall infiltration, pore water pressure evolution, and long-term deformation. Due to its robust numerical framework and user-friendly interface, PLAXIS 2D has become a standard tool in both academic research and engineering practice for simulating complex geotechnical systems.

2.1.1. Geotechnical Parameters and Constitutive Model

The Mohr–Coulomb constitutive model is a commonly used model in geotechnical engineering to describe soil and rock behavior. The adoption of the Mohr–Coulomb model allows for a clear comparison with analytical solutions based on elastic cavity theory, thereby facilitating the validation of the numerical results. It is based on a linear relationship between shear strength and effective normal stress, expressed as:

$$\tau = c + \sigma' \tan \phi \quad (1)$$

where, c is cohesion and ϕ is the friction angle.

The model assumes elastic–perfectly plastic behavior, meaning the material behaves elastically up to failure and then deforms plastically without additional strength gain. The elastic response is defined by Young's modulus and Poisson's ratio, while the plastic response is controlled by c, ϕ, and the dilation angle. Due to its simplicity and limited input parameters, the Mohr–Coulomb model is widely used in numerical analyses such as FEM. However, it does not account for stress-dependent stiffness or nonlinear soil behavior, which may limit its accuracy in complex conditions. The geotechnical parameters are shown in Table 1. Table 2 shows the shotcrete and lining properties.

Table 1. The rock parameters

The parameter	C (kPa)	E (kPa)	Phi (degree)	υ	λ (kN/m^3)
Rock	120	1300000	22	0.35	18
Fault material	15	10000	10	0.3	18

Table 2. The tunnel support parameters

The parameter	EA (kN/m)	EI (kNm^2/m)	υ
The shotcrete	5000000	16700	0.2
Concrete lining	14000000	187000	0.2

2.1.2. The Numerical Model Conditions

The numerical model was established with carefully defined boundary conditions to ensure realistic simulation of soil–structure interaction and to minimize boundary-induced effects. The lateral boundaries were restrained in the horizontal direction while remaining free in the vertical direction, whereas the bottom boundary was fully fixed to prevent both horizontal and vertical displacements. To avoid artificial constraint effects, the model domain was extended sufficiently far from the tunnel, with the lateral boundaries located at a distance of at least 4–6 times the tunnel diameter from the tunnel axis and the bottom boundary positioned at a depth exceeding 3–4 times the tunnel diameter. A mesh sensitivity analysis was conducted to ensure numerical accuracy, whereby different mesh densities were tested and the results were compared in terms of settlement and pore water pressure. The findings indicated that a refined mesh around the tunnel and fault zones was necessary to capture stress redistribution and deformation gradients accurately, while a coarser mesh could be used in regions farther from the area of interest without compromising solution stability.

In addition, a coupled hydro-mechanical analysis was adopted to simulate the influence of rainfall infiltration on ground response. The rainfall was applied as a constant flux boundary condition at the ground surface, with an intensity of 0.1 m/day over a duration of 0.1 day. This approach allowed for the evaluation of transient pore water pressure development and its interaction with the mechanical behavior of the soil–fault–tunnel system. The coupled analysis framework enables a more realistic representation of field conditions, particularly in assessing the combined effects of rainfall infiltration and excavation-induced stress changes on slope stability and deformation behavior. Figure 1 shows the FEM models with the boundary conditions.

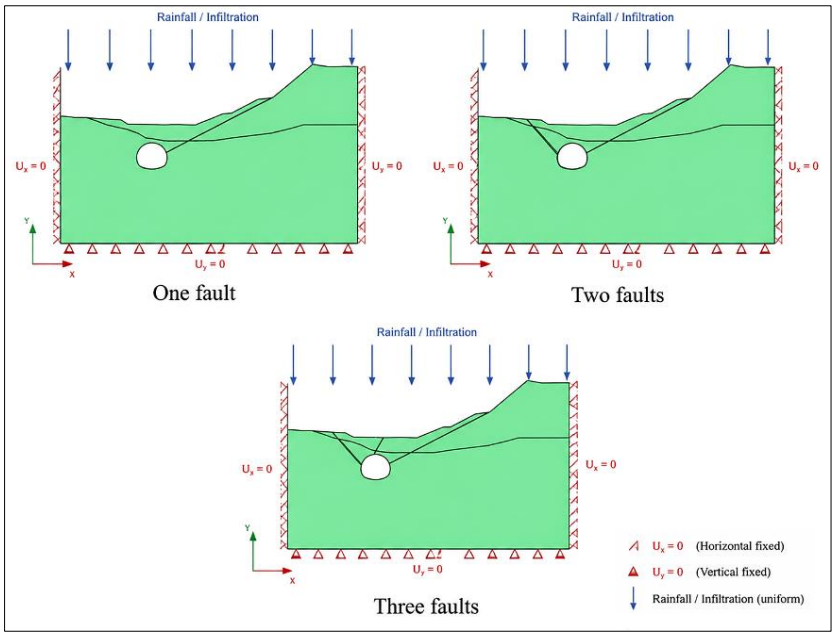

Figure 1. The FEM models

2.2. The Analytical Solution

Tunnel excavation inevitably induces stress redistribution within the surrounding ground, leading to deformation of both the tunnel boundary and the surrounding soil or rock mass. Analytical approaches have long been employed to estimate tunnel-induced ground movements because they provide rapid and physically interpretable predictions compared with numerical simulations. The analytical framework illustrated in the provided figures decomposes tunnel deformation into two primary mechanisms: uniform radial convergence and ovalization of the tunnel cross-section. These two deformation modes are treated as independent elastic responses and are subsequently combined using the principle of superposition to obtain the total displacement field around the tunnel. This approach allows efficient prediction of ground settlement patterns and tunnel deformation, particularly when multiple tunnels are constructed in proximity. Liu et al. (2022) [33] employed an analytical solution to evaluate the settlement behavior of twin tunnels through the superposition of individual tunnel settlement responses.

The analytical solution employed in this study is developed based on the classical framework of elastic cavity theory, which requires several simplifying assumptions in order to obtain closed-form expressions for stress redistribution and ground displacement around the tunnel. First, the surrounding ground is assumed to be homogeneous and isotropic, meaning that its mechanical properties are spatially uniform and independent of direction. Second, the soil or rock mass is considered to behave as a linear elastic continuum, where stress and strain are related through Hooke's law and no plastic yielding occurs within the analyzed deformation range. Third, the tunnel cross-section is assumed to be circular prior to excavation, which allows the analytical solution to exploit axisymmetric conditions in the elastic response of the ground. Furthermore, the ground layers are assumed to be horizontally stratified, ensuring that the initial stress field varies primarily with depth and can be represented by vertical and horizontal in-situ stresses. The analytical formulation also assumes that the induced deformations remain small relative to the tunnel radius, thereby allowing linear elasticity theory and geometric linearization to remain valid. Finally, when multiple tunnels are present, their interaction effects are approximated using the principle of linear superposition, whereby the total displacement field is obtained as the sum of the individual displacement contributions generated by each tunnel.

Under these assumptions, closed-form analytical expressions can be derived to describe both the redistribution of stresses and the resulting displacement field around the excavated tunnel. The analytical model requires a set of geometric, mechanical, and hydraulic parameters describing the tunnel and surrounding ground. The analytical solution for tunnel-induced ground displacement requires a set of geometric, mechanical, and hydraulic parameters describing both the tunnel and the surrounding ground. Based on the previously mentioned issues, the present analytical framework provides a simplified yet physically interpretable approach for evaluating tunnel-induced ground deformation in multi-tunnel systems. Compared with full numerical simulations, the proposed method offers several advantages, including reduced computational cost, rapid estimation capability, and clearer identification of the dominant deformation mechanisms governing tunnel–ground interaction. By decomposing tunnel deformation into radial convergence and ovalization components, the analytical model enables independent evaluation of the effects of isotropic stress release and deviatoric stress redistribution around the excavation boundary. This decomposition improves the physical interpretation of settlement formation and facilitates the assessment of interaction effects between adjacent tunnels.

The key geometric parameters include the tunnel diameter D, from which the tunnel radius is obtained as:

$$R = \frac{D}{2} \tag{2}$$

as well as the tunnel axis depth $H$and the groundwater level (GWL). These parameters define the spatial configuration of the tunnel within the ground mass and determine the initial stress conditions acting on the excavation. The mechanical behavior of the surrounding soil or rock mass is characterized by several material properties, including the dry and saturated unit weights γ_{dry} and γ_{sat}, Young's modulus E, Poisson's ratio ν, cohesion c, and the internal friction angle ϕ. These parameters describe the stiffness and shear strength of the ground and govern its response to stress redistribution during excavation.

From the elastic constants, the shear modulus Gcan be derived as:

$$G = \frac{E}{2(1+\nu)} \tag{3}$$

which represents the resistance of the ground to shear deformation. In addition, the coefficient of earth pressure at rest is defined as:

$$K_0 = \frac{\sigma_h}{\sigma_v} \tag{4}$$

where σ_v and σ_h denote the vertical and horizontal in-situ stresses, respectively. This coefficient describes the relationship between horizontal and vertical stresses in the ground prior to excavation. Before tunnel excavation, the vertical effective stress at the tunnel depth can be estimated as:

$$\sigma_v' = \gamma H \tag{5}$$

where, γ represents the unit weight of the soil. When the ground is saturated, the effective stress must account for buoyancy effects, and the expression becomes:

$$\sigma_v' = (\gamma_{sat} - \gamma_w)H \quad (6)$$

where, γ_w is the unit weight of water. The horizontal effective stress is then calculated using the earth pressure coefficient:

$$\sigma_h' = K_0\sigma_v' \quad (7)$$

The pore water pressure distribution also influences the effective stress state around the tunnel. The pore pressure at a depth $h$below the groundwater table is given by:

$$p_w = \gamma_w h \quad (8)$$

where, p_w represents the hydrostatic water pressure.

Tunnel excavation results in stress redistribution and deformation of the surrounding ground. In this analytical framework, the deformation is represented by two primary mechanisms: uniform radial convergence and tunnel ovalization.

Uniform convergence corresponds to the axisymmetric contraction of the tunnel boundary caused by stress release following excavation. According to elastic cavity theory, the maximum radial convergence at the tunnel boundary can be approximated by:

$$U_{conv,max} = \frac{(1+\nu)}{E}(\sigma_v' - p_i)R \quad (9)$$

where, p_i represents the internal pressure acting at the tunnel boundary, which may correspond to support pressure or lining pressure, and $R$is the tunnel radius. This deformation mode produces a uniform inward displacement of the tunnel wall while maintaining its circular geometry. In contrast, tunnel ovalization occurs when vertical and horizontal stresses are unequal. The stress difference leads to elliptical distortion of the tunnel cross-section. The deviatoric stress responsible for this deformation is expressed as:

$$p_0 = \sigma_v' - \sigma_h' \quad (10)$$

The maximum displacement associated with ovalization can be estimated as:

$$U_{oval,max} = \frac{p_0 R}{2G} \quad (11)$$

This deformation causes differential displacement along the tunnel perimeter, resulting in elongation along one axis and contraction along the perpendicular axis. To evaluate the displacement field in the surrounding ground, a spatial grid of coordinates (x, y) is generated. For each point within this grid, the radial distance from the tunnel center is determined by:

$$r = \sqrt{x^2 + y^2} \quad (12)$$

The displacement components due to convergence and ovalization are calculated independently. The radial displacement induced by convergence decreases with increasing distance from the tunnel and can be expressed as:

$$u_{conv}(r) = U_{conv,max}\left(\frac{R}{r}\right) \quad (13)$$

The displacement caused by ovalization depends on both radial distance and angular position relative to the tunnel center. It can be written as:

$$u_{oval}(r,\theta) = U_{oval,max}\left(\frac{R}{r}\right)^2 \cos(2\theta) \quad (14)$$

where, θ denotes the polar angle measured from the horizontal axis.

The total displacement at any point around the tunnel is obtained by summing the two displacement components according to the principle of superposition:

$$Z(x,y) = u_{conv}(x,y) + u_{oval}(x,y) \quad (15)$$

This combined displacement field describes both the settlement and distortion patterns induced by tunnel excavation. When multiple tunnels are present, the interaction between them can also be evaluated using linear superposition, assuming that the ground response remains within the elastic range. For a system consisting of three tunnels, the total vertical and horizontal displacements can be expressed as:

$$U_{Y_{tot}} = U_{Y1} + U_{Y2} + U_{Y3} \quad (16)$$

$$U_{X_{tot}} = U_{X1} + U_{X2} + U_{X3} \quad (17)$$

where, U_{Yi} and U_{Xi} denote the vertical and horizontal displacement components induced by the i^{th} tunnel. Furthermore, the vertical settlement associated with each individual tunnel can be decomposed into contributions from convergence and ovalization mechanisms:

$$U_Y = U_{yc} + U_{yo} \tag{18}$$

where, U_{yc} represents settlement induced by radial convergence and U_{yo} represents settlement induced by tunnel ovalization. Together, these components provide a comprehensive analytical representation of tunnel-induced ground deformation and enable efficient prediction of settlement patterns in multi-tunnel systems. Figure 2 shows the proposed analytical solution flow chart.

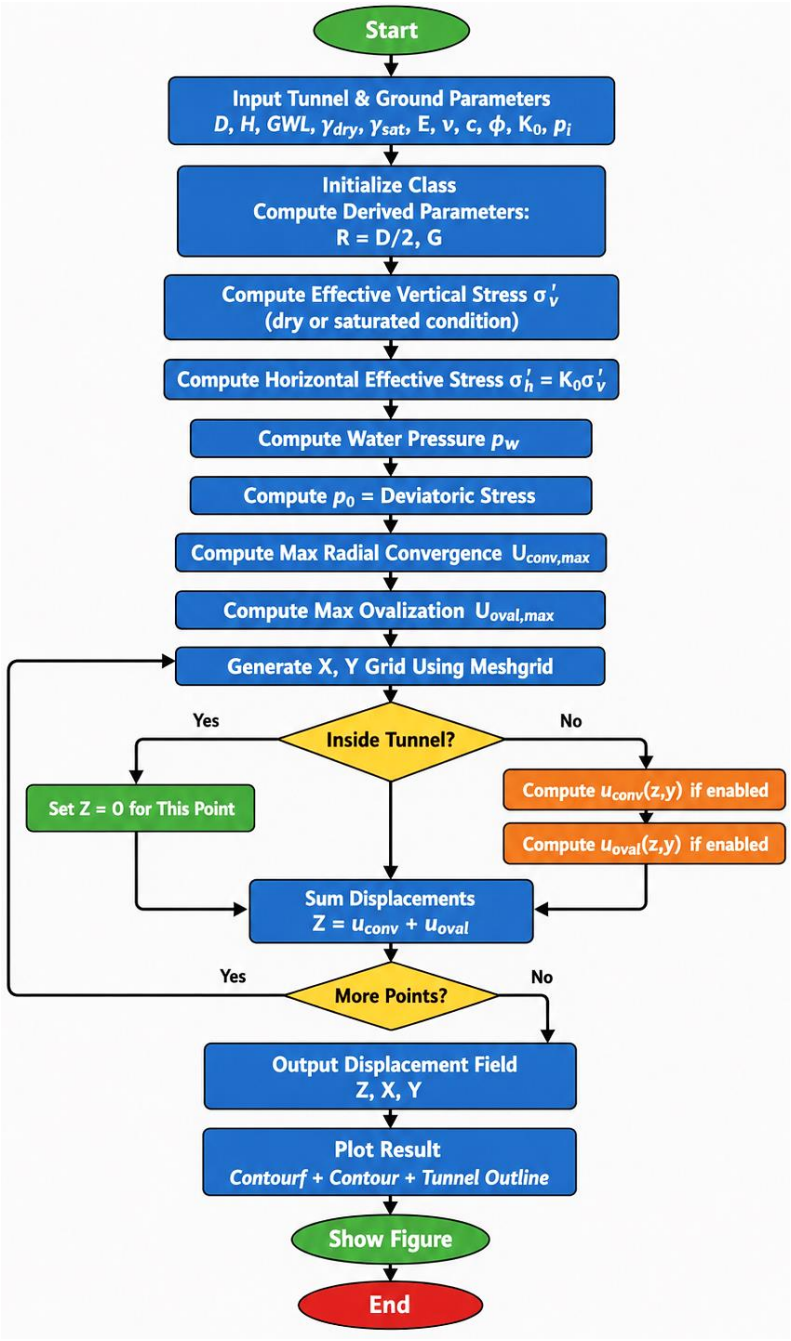

Figure 2. The analytical solution flow chart

3. Results

3.1. The Validation Process

To assess the reliability of the proposed analytical solution for predicting tunnel-induced settlement, a comparison was conducted with numerical results obtained using PLAXIS 2D. The numerical model was developed using the finite

element method under plane strain conditions, with the same geometric configuration and soil parameters adopted in the analytical formulation. The tunnel settlement and displacement field predicted by the analytical solution were calculated using the derived equations for uniform radial convergence and tunnel ovalization, and the results were compared with the numerical outputs from PLAXIS 2D. The comparison indicates that the analytical model captures the general trend and magnitude of tunnel-induced settlement with reasonable accuracy. Minor differences can be attributed to the simplifying assumptions of linear elasticity in the analytical solution, whereas the numerical model accounts for more complex stress redistribution. Overall, the results demonstrate that the analytical approach provides a satisfactory approximation for estimating tunnel settlement and can be effectively used for preliminary analysis. Figure 3-a shows the contour deformation for the analytical solution and finite element method. While Figure 3-b shows the curves above the tunnel.

To provide a quantitative assessment of the agreement between the analytical solution and FEM simulation, the Root Mean Square Error (RMSE) and maximum percentage difference were calculated along the section.

$$RMSE = \sqrt{\frac{1}{n}\sum_{i=1}^{n}\left(S_{FEM,i} - S_{Analytical,i}\right)^2} \quad (19)$$

$$Max\ \%\ Difference = \max\left(\frac{|S_{FEM,i} - S_{Analytical,i}|}{S_{Analytical,i}} \times 100\%\right) \quad (20)$$

where, $S_{FEM,i}$ and $S_{Analytical,i}$ are the settlement values at point i from FEM and analytical solutions, respectively, and n is the total number of points along the section.

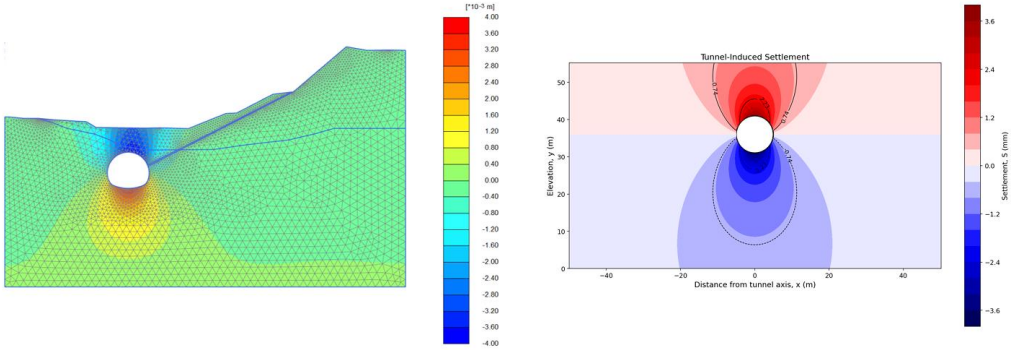

Numerical Simulation
FEM analysis

Analytical Solution

(a) The contour settlement for the FEM and the analytical solution

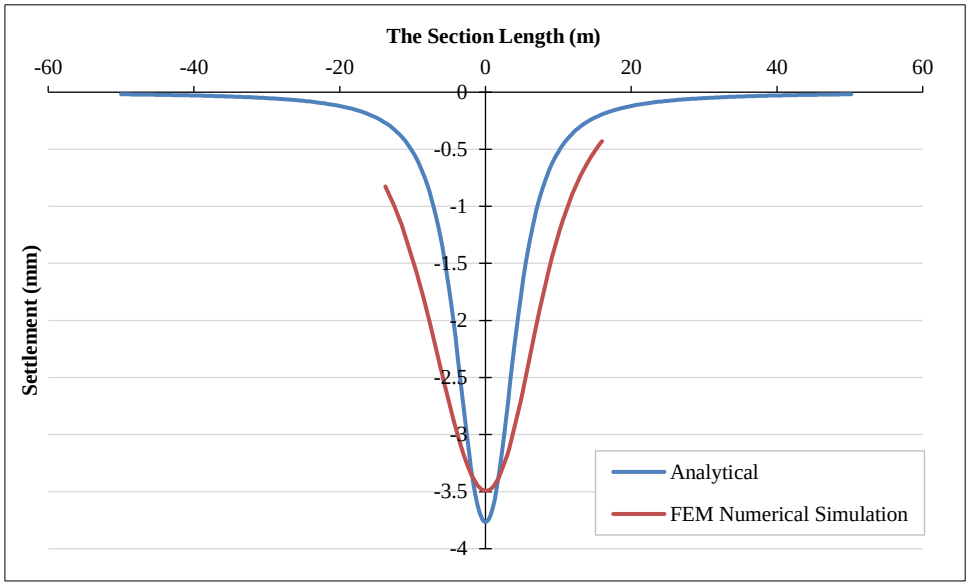

(b) The chart comparison between FEM and analytical solution

Figure 3. The comparison between numerical simulation and analytical solution

For the current model, the computed RMSE is 0.12 mm, and the maximum percentage difference is 7.5%, indicating that the FEM simulation reproduces the analytical solution with high fidelity. These metrics confirm that the numerical model provides an accurate representation of the theoretical settlement profile while accounting for minor deviations due to discretization and boundary effects.

3.2. Parametric Study

In this parametric study, the presence of faults within the rock mass was explicitly incorporated into the modeling framework. Each fault was idealized as a zone of weakened material embedded within the intact rock, thereby reflecting its reduced mechanical properties relative to the surrounding medium. The analysis considered different fault configurations, including one, two, and three fault scenarios, in order to evaluate the influence of fault quantity on the overall mechanical response. In addition, various fault orientations were examined to assess the effect of directional variability on system behavior. The mechanical properties assigned to the fault material are summarized in Table 2. In the subsequent sections, parametric variations are performed with respect to the key mechanical properties of the fault material, namely the modulus of elasticity, cohesion, and friction angle. Two main sections are considered to investigate the influence of these properties on settlement and pore water pressure.

3.2.1. Modulus of Elasticity Variation

Three representative values of the modulus of elasticity were considered in this study, namely $E = 10{,}000$kPa, $E = 8{,}000$kPa, and $E = 6{,}000$kPa. Figure 4 illustrates the results corresponding to the case where $E = 10{,}000$kPa. Figure 4-a shows the settlement along the fault. While Figure 4-b shows the settlement above the tunnel. Figure 5-a shows the pore water pressure along the fault. While Figure 5-b shows the pore water pressure above the tunnel. With regard to settlement, the results indicate a clear increasing trend with the number of faults. Specifically, within the fault zone, the settlement values increased from 4 mm to 9 mm and 14 mm as the number of faults increased from one to three, respectively. A similar trend was observed in the section located above the tunnel. Where settlement also increased with the number of faults. Additionally, the variation in pore water pressure is relatively limited, particularly along the fault zone, where only minor differences are observed. However, more noticeable variations are evident in the section above the tunnel. When the modulus of elasticity is reduced to $E = 8{,}000$kPa, the results show that settlement continues to increase with the number of faults (Figure 6-a and Figure 6-b). The maximum settlement above the tunnel ranges between 10 mm and 40 mm, compared to a range of 7 mm to 30 mm for $E = 10{,}000$ kPa, indicating that lower stiffness leads to greater deformation. In terms of pore water pressure, the section located along the fault exhibits values ranging from 50 kPa to 500 kPa when $E = 10{,}000$kPa.

This range increases to 50 kPa to 600 kPa when $E = 8{,}000$ kPa Figure 7-a and Figure 7-b, suggesting that a reduction in the modulus of elasticity results in higher pore water pressure. Conversely, in the section above the tunnel, pore water pressure values are relatively low, with an average range between 0 kPa and 60 kPa. With a further reduction in the modulus of elasticity to $E = 6{,}000$kPa, the results indicate that, in the section along the fault, the settlement values for two and three faults are nearly identical. Moreover, the difference between the cases of one fault and multiple faults (two or three) becomes less pronounced. However, the overall trend of settlement distribution changes, and the location of the maximum settlement shifts. A similar behavior is observed in the section above the tunnel, with one notable distinction: in the case of a single fault, the settlement remains relatively smaller compared to the scenarios involving two or three faults. Figure 8-a and Figure 8-b show the settlement in the fault and above the tunnel when the modulus of elasticity is 6000 kN/m^2. Also, Figures 9-a and 9-b show the pore water pressure when the modulus of elasticity is 6000 kN/m^2.

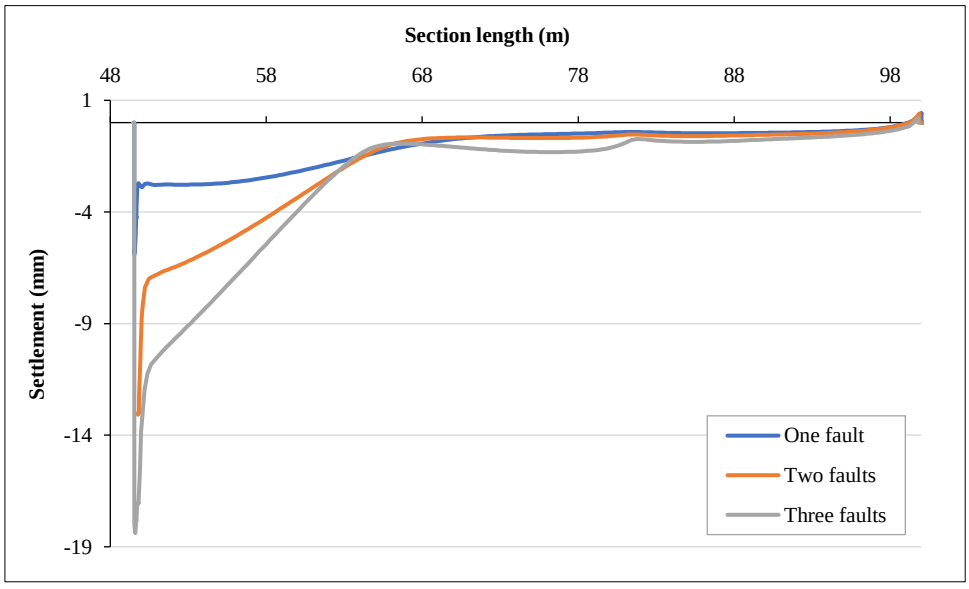

(a)

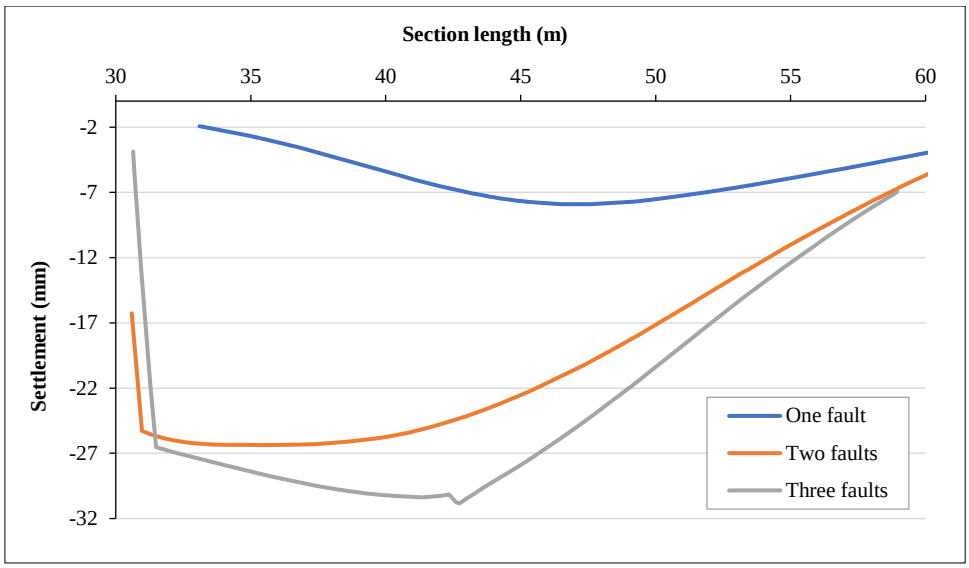

(b)

Figure 4. The settlement when the Modulus of Elasticity is 10000 kN/m^2; (a) Along the fault, (b) Above the tunnel

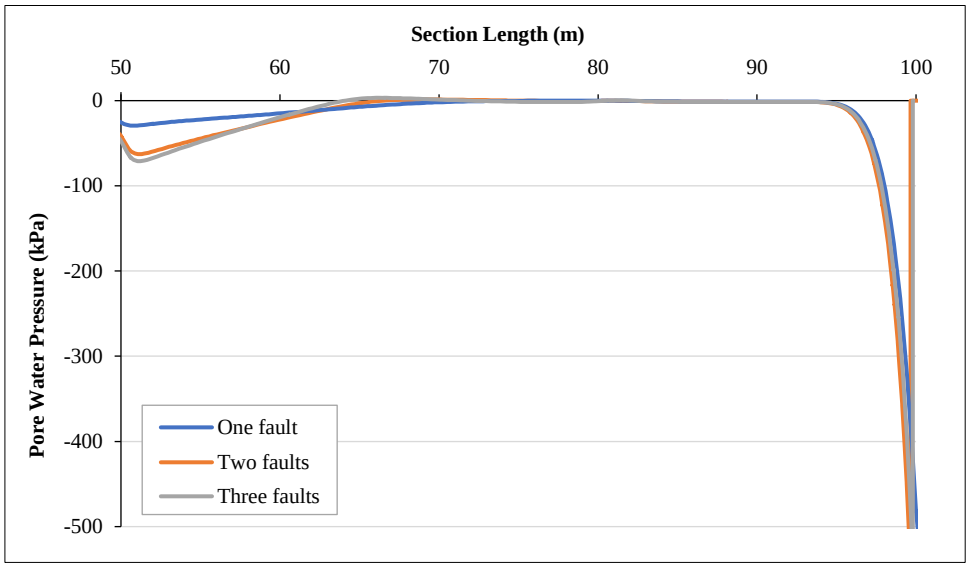

(a)

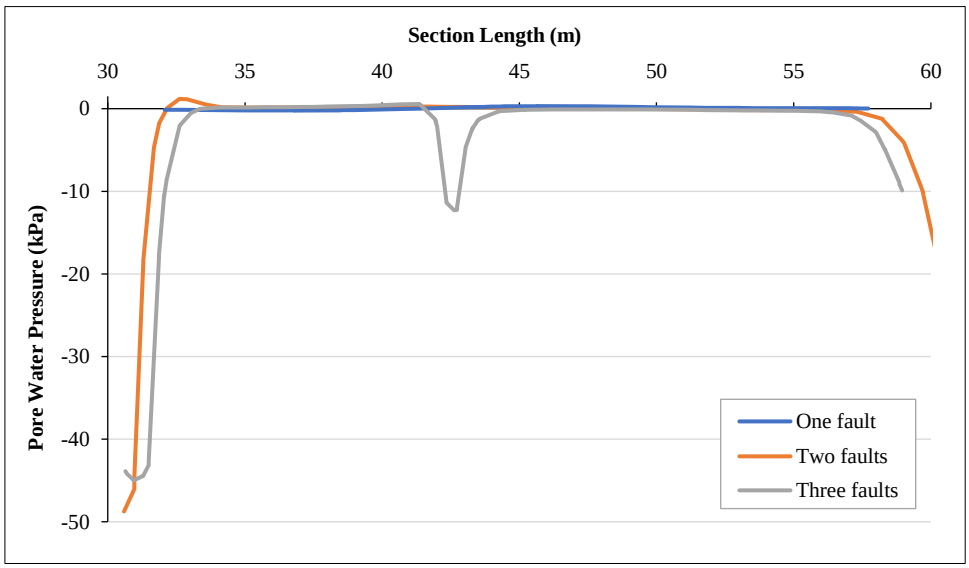

(b)

Figure 5. The pore water pressure when the Modulus of Elasticity is 10000 kN/m^2; (a) Along the fault, (b) Above the tunnel

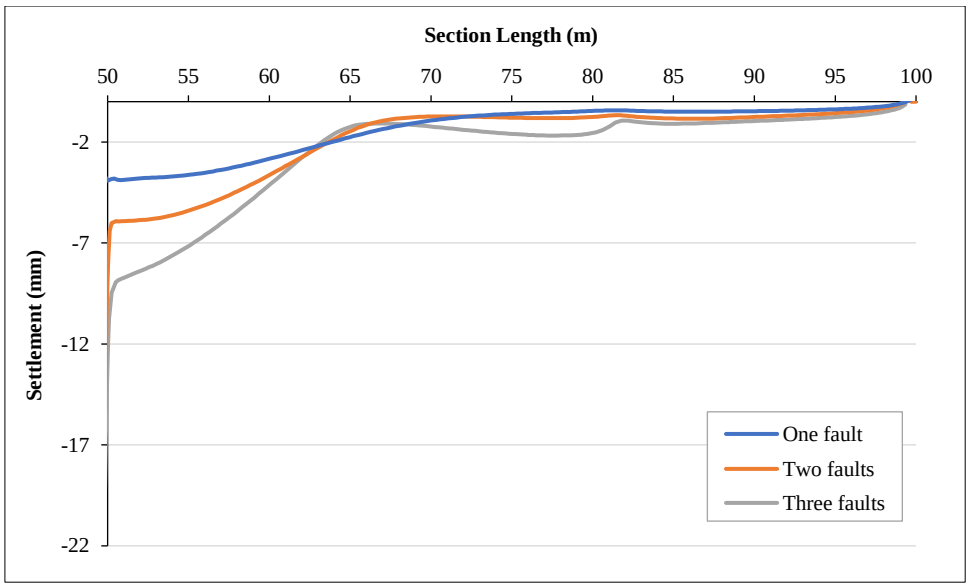

(a)

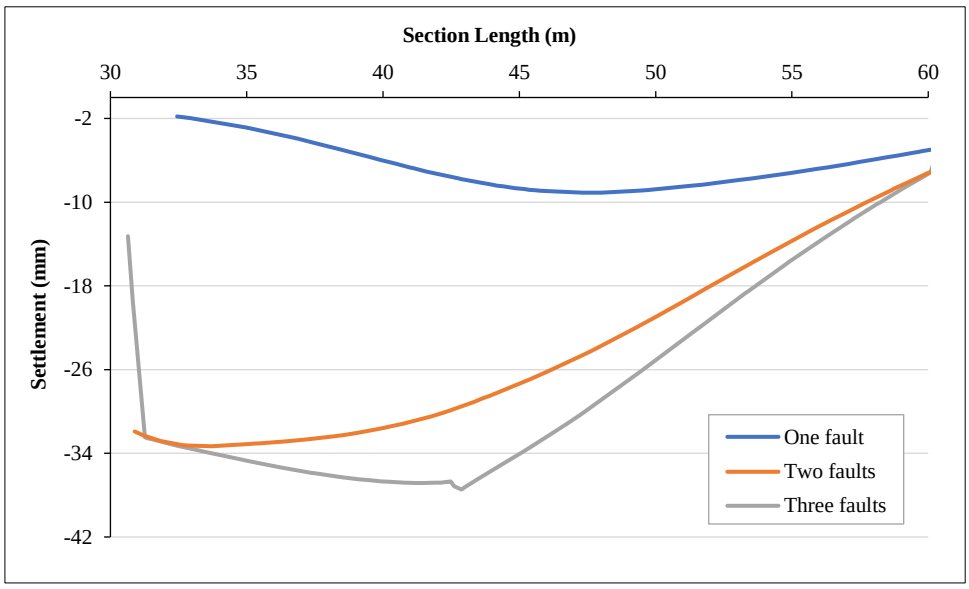

(b)

Figure 6. The settlement when the Modulus of Elasticity is 8000 kN/m^2; (a) Along the fault, (b) Above the tunnel

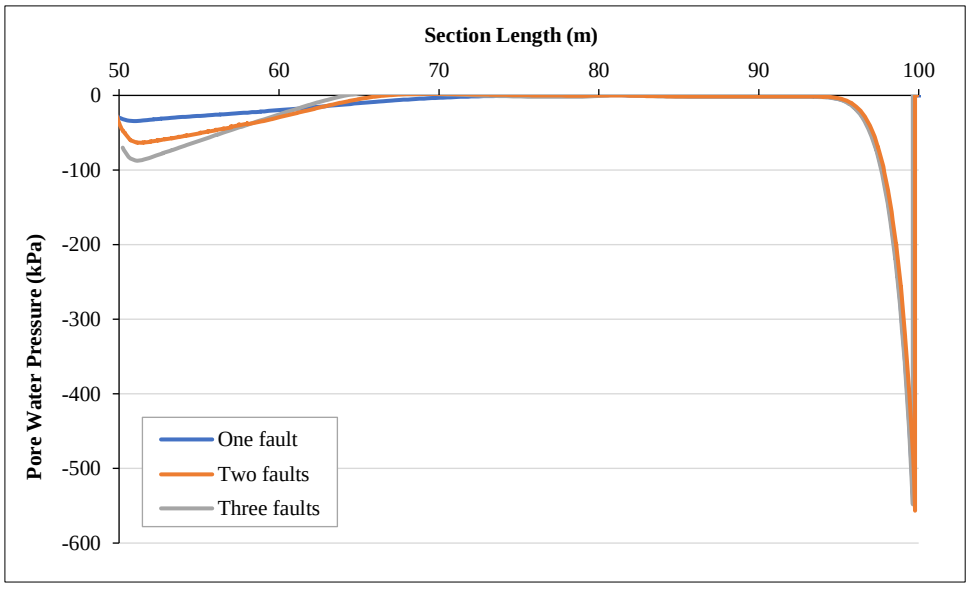

(a)

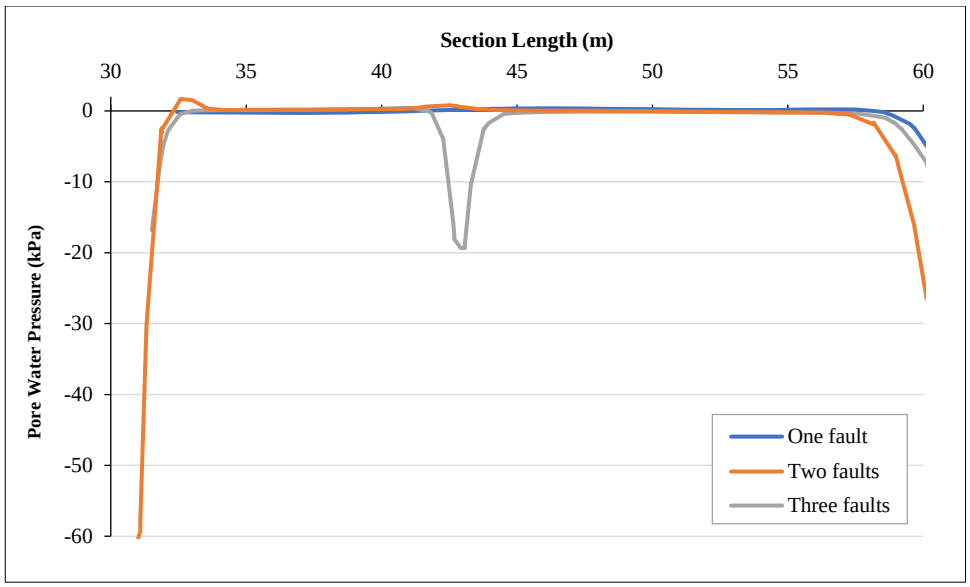

(b)

Figure 7. The pore water pressure when the Modulus of Elasticity is 8000 kN/m^2; (a) Along the fault, (b) Above the tunnel

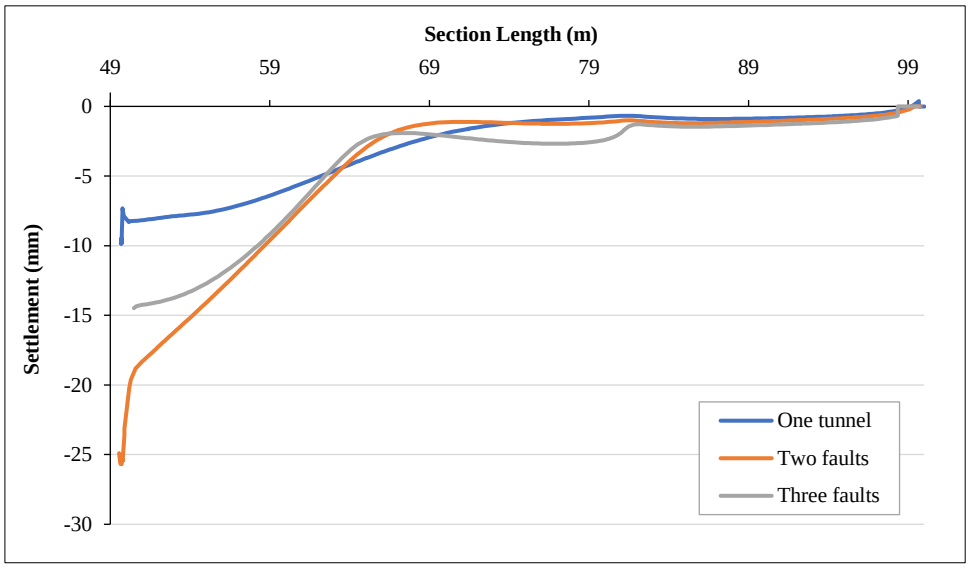

(a)

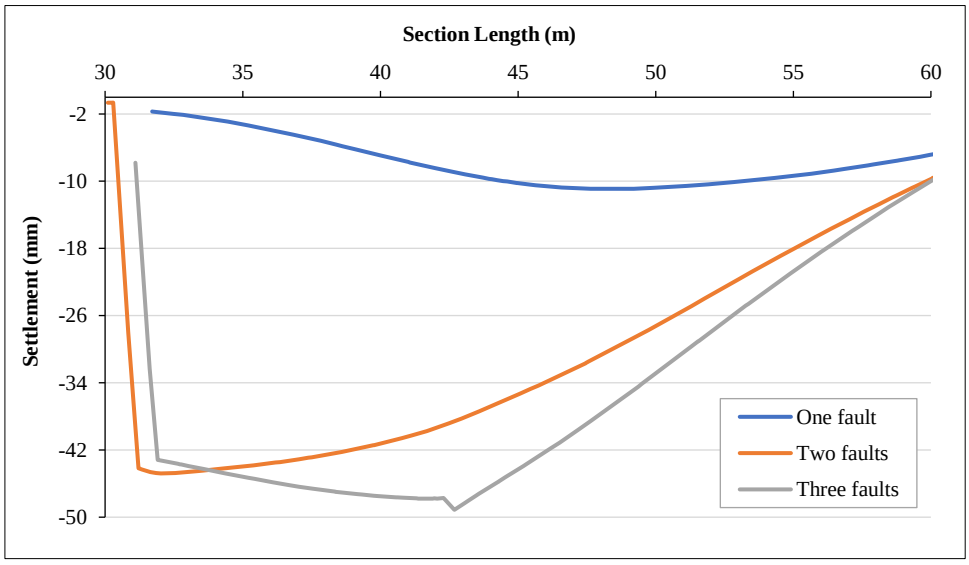

(b)

Figure 8. The settlement when the Modulus of Elasticity is 6000 kN/m^2; (a) Along the fault, (b) Above the tunnel

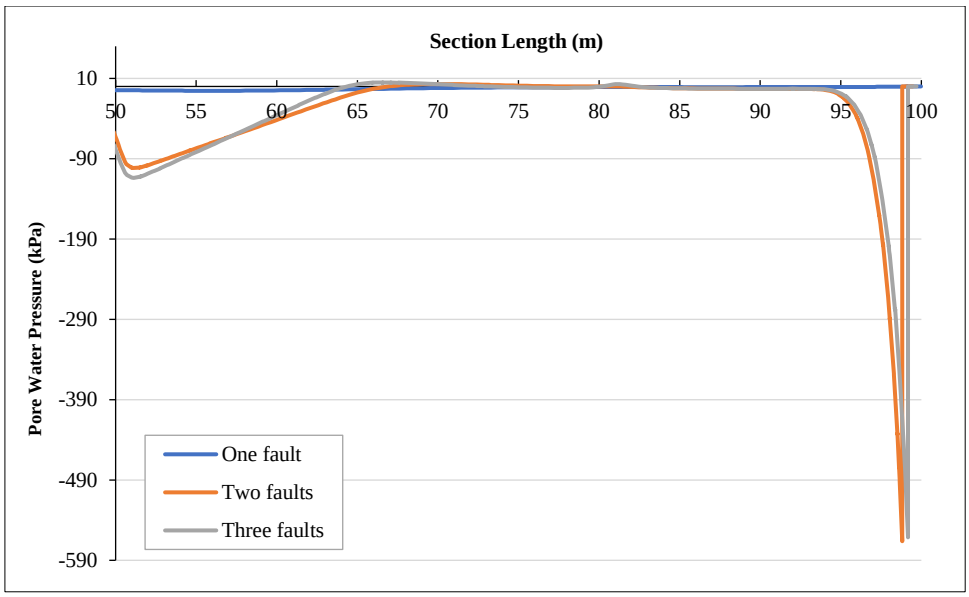

(a)

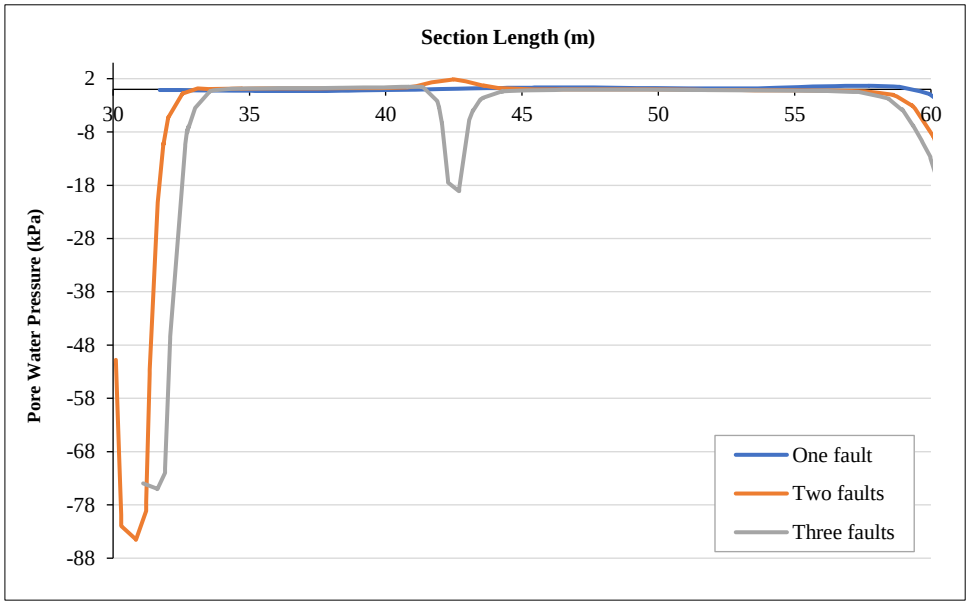

(b)

Figure 9. The pore water pressure when the Modulus of Elasticity is 6000 kN/m^2; (a) Along the fault, (b) Above the tunnel

A comparison of pore water pressure values under varying modulus of elasticity of the fault material indicates that the differences are relatively minor. In contrast, the most significant variations are observed in the settlement response, which is markedly influenced by changes in the modulus of elasticity. The relatively minor variation in pore water pressure with changes in the modulus of elasticity can be attributed to the fact that pore pressure is primarily governed by hydraulic conditions, such as permeability and boundary conditions, rather than mechanical stiffness [34]. In contrast, the modulus of elasticity plays a critical role in controlling the mechanical response of the material [35]. As the modulus decreases, the fault zone becomes softer and more deformable, leading to greater strain under the same stress conditions. This results in significant increases in settlement, while the pore water pressure remains comparatively unaffected. Consequently, the observed behavior reflects a decoupled response, in which hydraulic parameters control pore pressure distribution, whereas mechanical properties predominantly influence deformation.

3.2.2. Cohesion Variation

As shown in Figure 10-a, it is evident that, in the section along the fault, there is no significant variation in settlement with changes in the number of faults. However, Figure 10-b indicates that, in the section above the tunnel, settlement increases with an increasing number of faults. Ghafari et al. (2020) [36] explained that the presence and

characteristics of faults increase deformation in soil masses, which in geotechnical engineering is a primary factor leading to greater settlement. A substantial difference is observed between the case of a single fault and those involving two or three faults, highlighting the pronounced influence of fault multiplicity on surface deformation. Furthermore, a comparison of settlement values for cohesion values of 10 kPa and 5 kPa reveals only minor differences in both magnitude and distribution trend. This suggests that, within the considered range, cohesion has a negligible influence on the mechanical response of the fault material. The pore water pressure does not show much difference in the two cases.

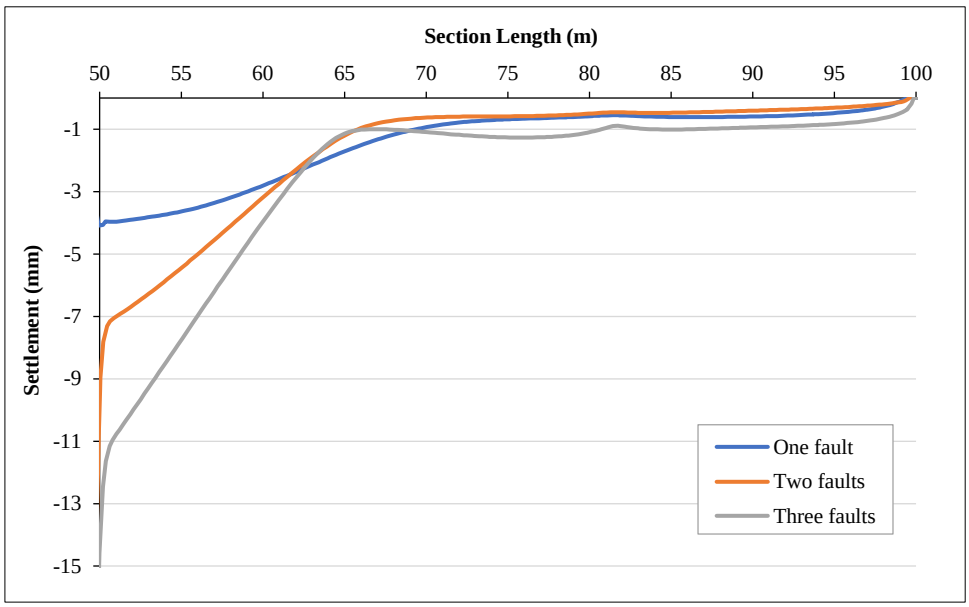

(a)

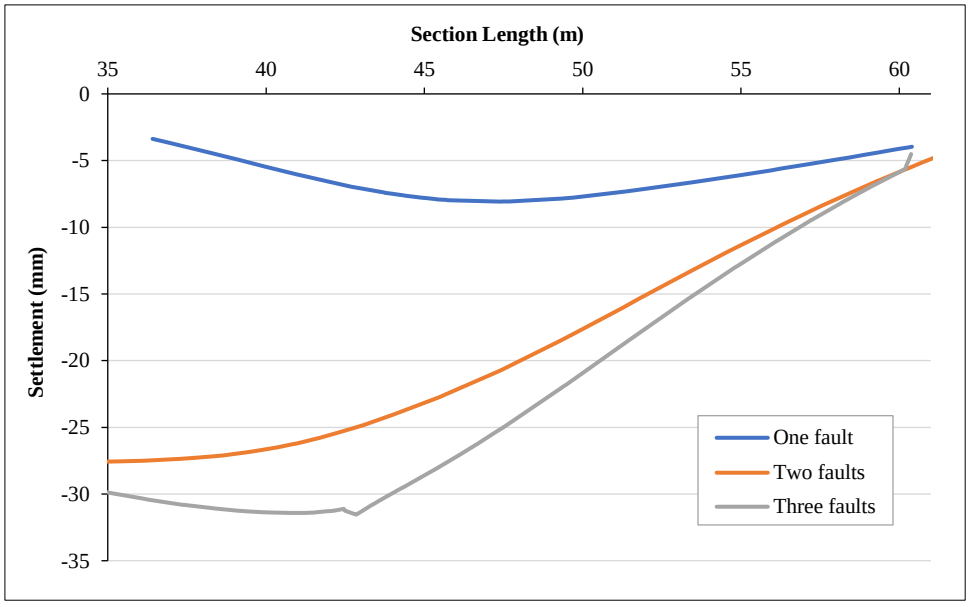

(b)

Figure 10. The settlement when the cohesion is 10 kN/m^2; (a) Along the fault, (b) Above the tunnel

Figure 11-a illustrates the distribution of pore water pressure along the fault section for cases with one, two, and three faults. The results indicate that the presence of multiple faults influences pore pressure behavior, particularly in the upstream portion of the section (45–65 m). The data indicate that the magnitude of pore water pressure in this section is relatively low, fluctuating around 0 kPa with slight negative pressures in localized areas (Figure 11-b). Notably, the case with three faults exhibits a small peak around 45 m, suggesting water concentration in the soil mass induced by fault-related discontinuities. In general, the differences among the one-fault, two-fault, and three-fault cases are minor, implying that pore pressure effects of faults above the tunnel are limited compared to those along the fault zone.

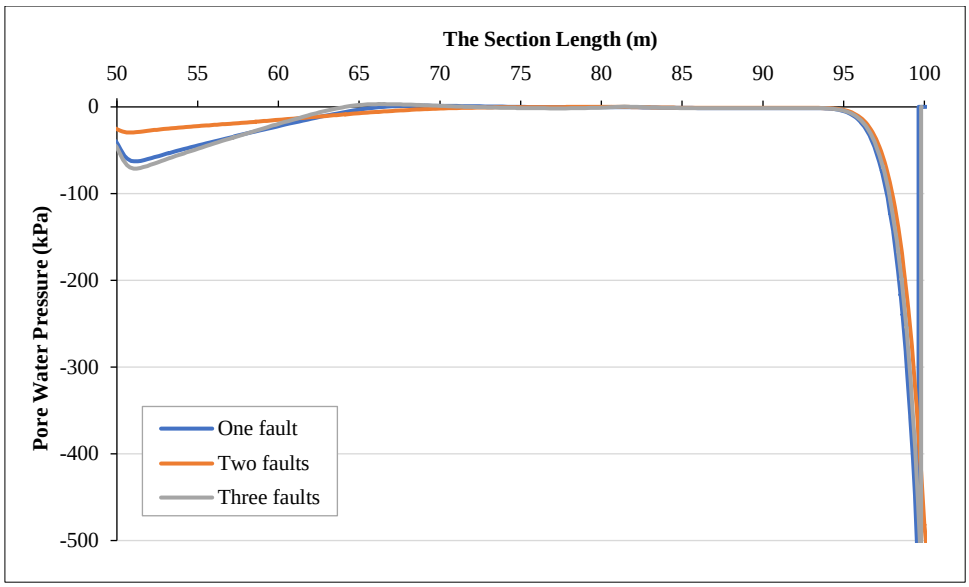

(a)

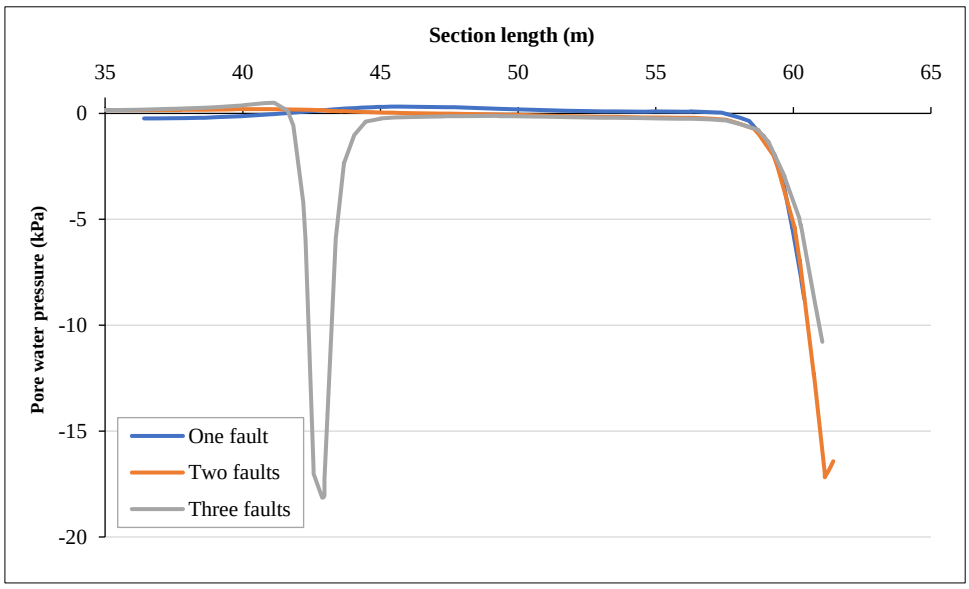

(b)

Figure 11. The pore water pressure when the cohesion is 10 kN/m^2; (a) Along the fault, (b) Above the tunnel

When the cohesion was reduced to 5 kN/m², the settlement along the faulted section exhibited notable differences depending on the number of faults present (Figure 12-a). Specifically, for the case of a single fault, the maximum settlement was approximately 4 mm. In contrast, when two or three faults were present, the settlement increased to around 9 mm. This increase can be attributed to the mechanical influence of the faults, which act as discontinuities within the soil mass, reducing stiffness and creating preferential deformation paths that amplify settlement under the applied load. The results underscore the significant role of fault density in controlling deformation behavior in faulted geomaterials. The influence of fault density becomes particularly pronounced in the section above the tunnel (Figure 12-b). For instance, when only a single fault is present, the maximum settlement reaches approximately 8 mm. This value increases substantially with additional faults: around 29 mm for two faults and nearly 35 mm for three faults.

These results indicate that the presence and number of faults significantly amplify settlement above the tunnel, likely due to the creation of multiple deformation paths and localized stress concentrations within the overlying soil mass. However, with regard to pore water pressure, the results indicate that there are no substantial differences between the two analyzed sections, either above the tunnel or along the fault zones. This suggests that, despite variations in fault number and friction angle, the overall pore pressure distribution remains relatively insensitive to these factors in the sections considered, highlighting the dominant influence of hydraulic boundary conditions and soil permeability over mechanical discontinuities in controlling pore pressure. Figure 13-a shows the pore water pressure along the fault. While, Figure 13-b shows the pore water pressure above the tunnel.

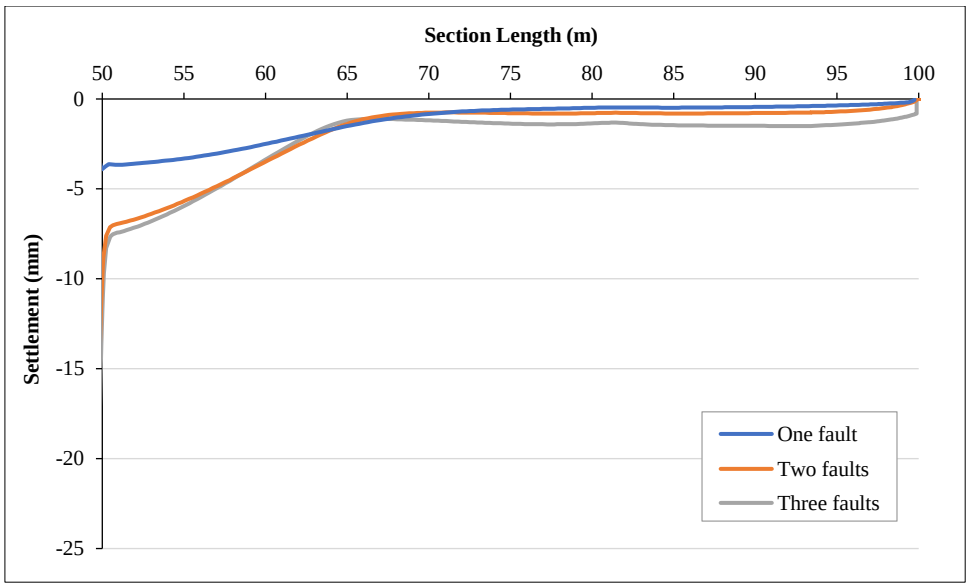

(a)

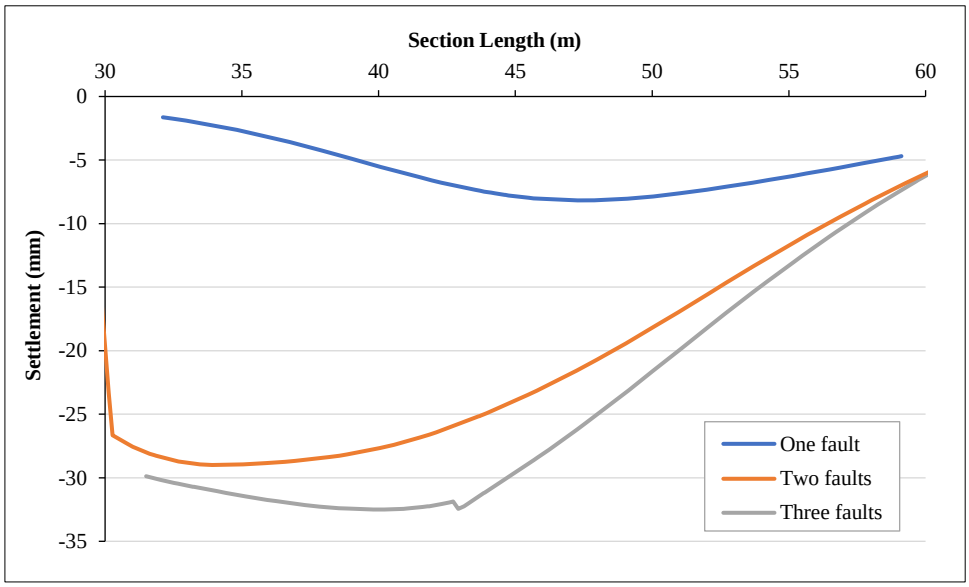

(b)

Figure 12. The settlement when the cohesion is 5 kN/m^2; (a) Along the fault, (b) Above the tunnel

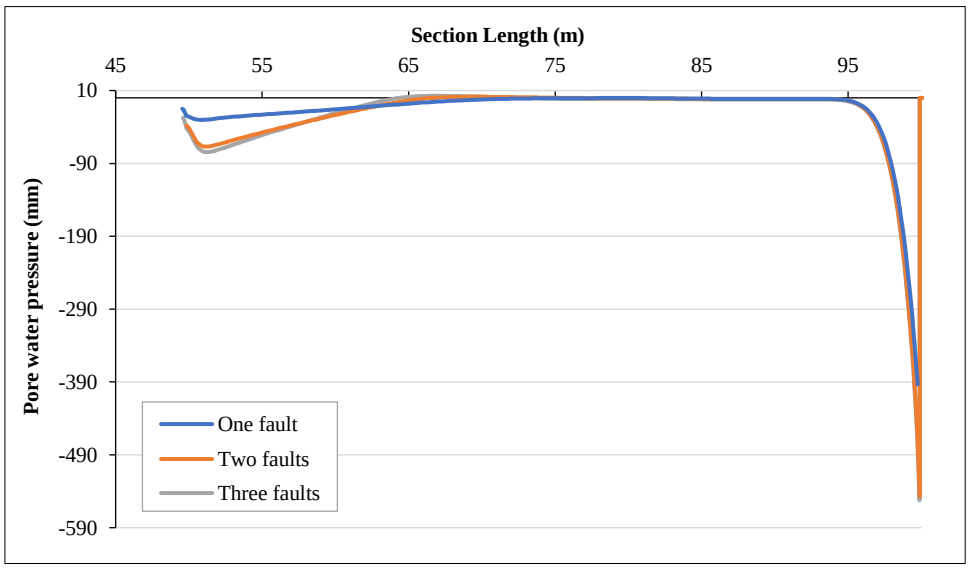

(a)

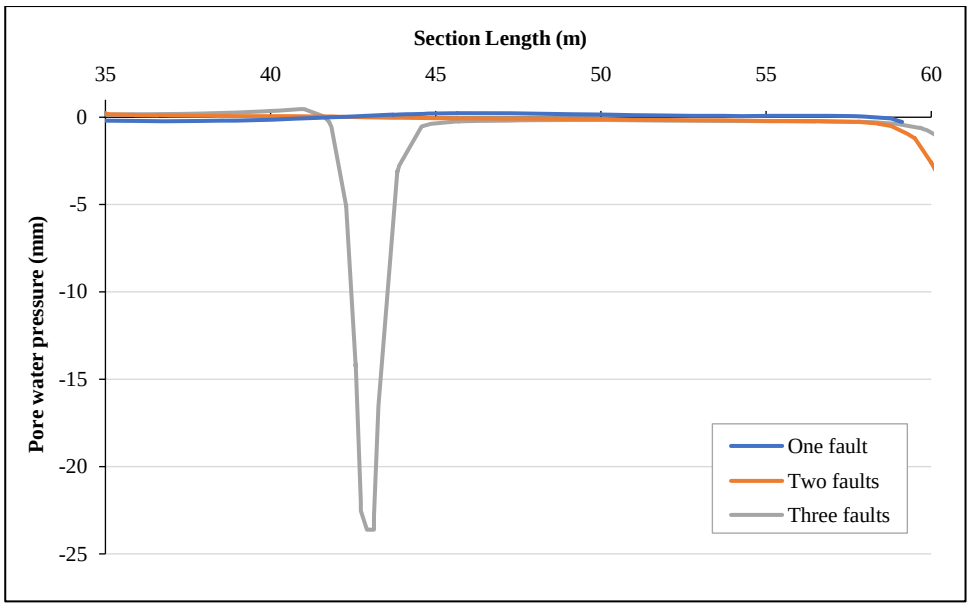

(b)

Figure 13. The pore water pressure when the cohesion is 5 kN/m^2; (a) Along the fault, (b) Above the tunnel

3.2.3. The Friction Angel Variation

In this section, the variation of the friction angle is systematically examined. Two representative values are considered, namely 8° and 6°, to evaluate their influence on soil behavior. The analysis focuses on two primary response parameters: surface settlement and pore water pressure. These parameters are selected to assess the mechanical and hydraulic responses of the soil system under different friction angle conditions. The results indicate that there is no significant variation in settlement between the two friction angle cases (Figure 14-a and Figure 14-b). Furthermore, the overall trend of settlement remains nearly identical under both conditions (Figure 15-a and Figure 15-b). Regarding the pore water pressure, the results indicate that when the friction angle is 8°, the maximum pore water pressure along the fault section occurs in the case of three faults, reaching approximately 79 kPa (Figure 16-a and Figure 16-b). In contrast, when the friction angle is reduced to 6°, the maximum pore water pressure in the same section decreases significantly, reaching only about 20 kPa (Figure 17-a and Figure 17-b). Perrone et al. (2008) [37] demonstrated how pore pressure distribution and shear strength parameters (including friction angle φ′) interact in slope/failure problems, which implicitly supports that changes in φ′ will affect pore pressure responses in mechanical models.

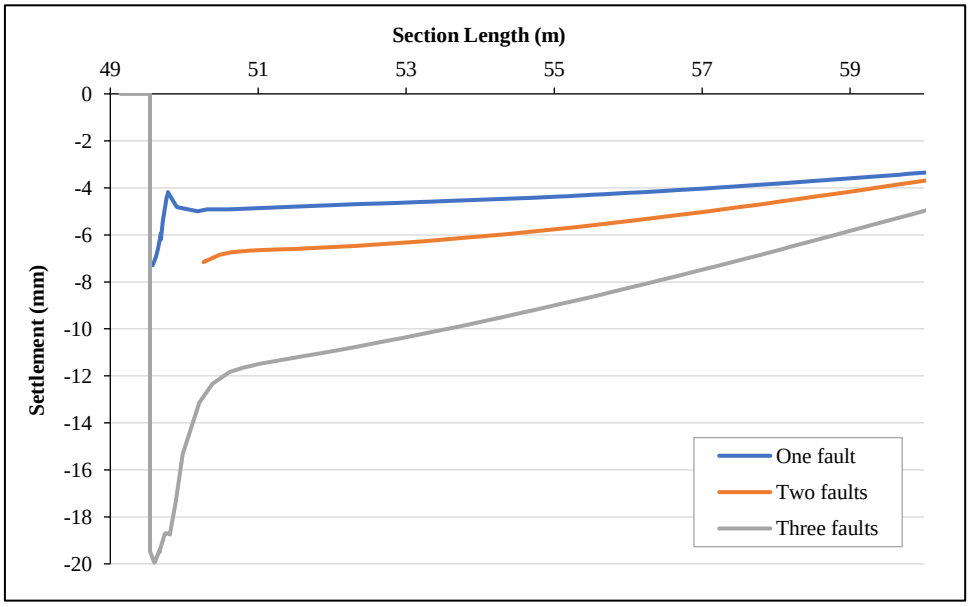

(a)

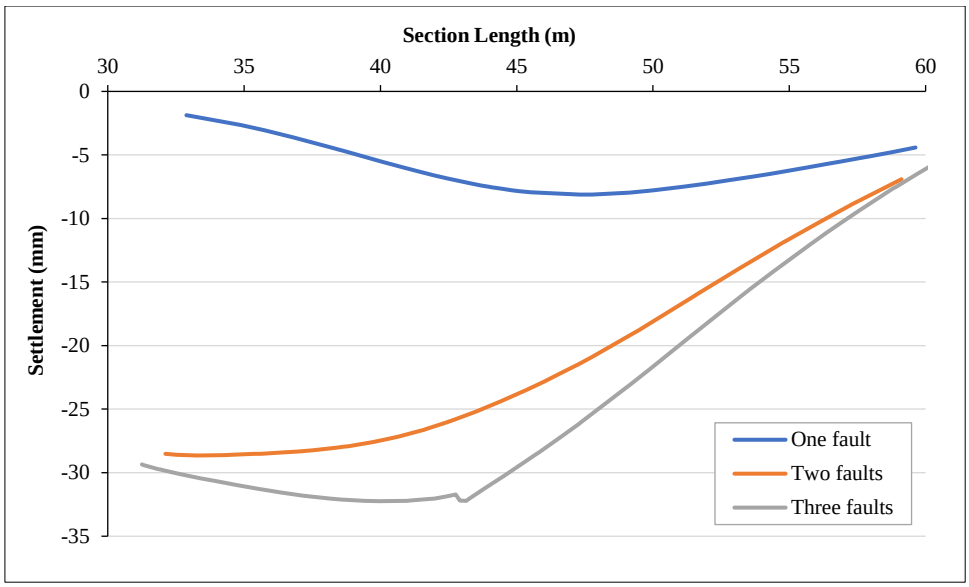

(b)

Figure 14. The settlement when the friction angel is 8; (a) Along the fault, (b) Above the tunnel

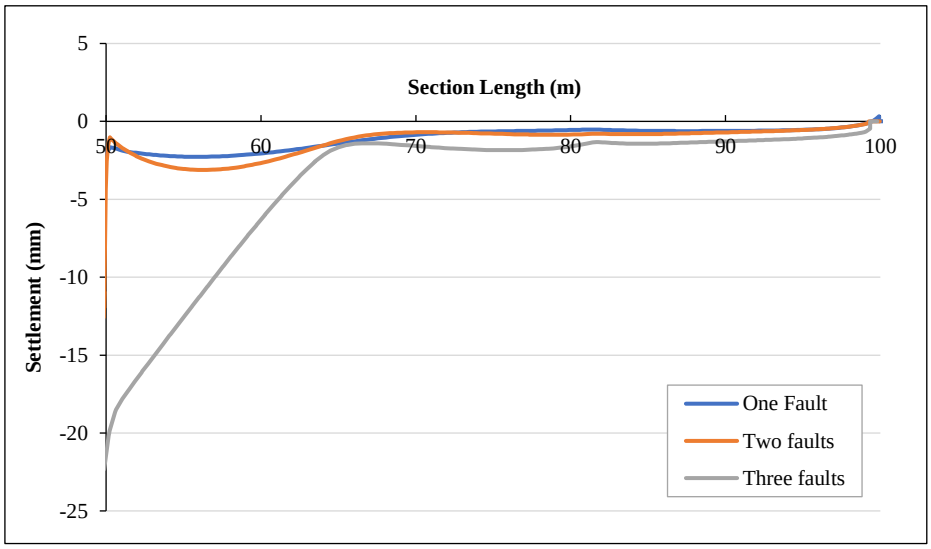

(a)

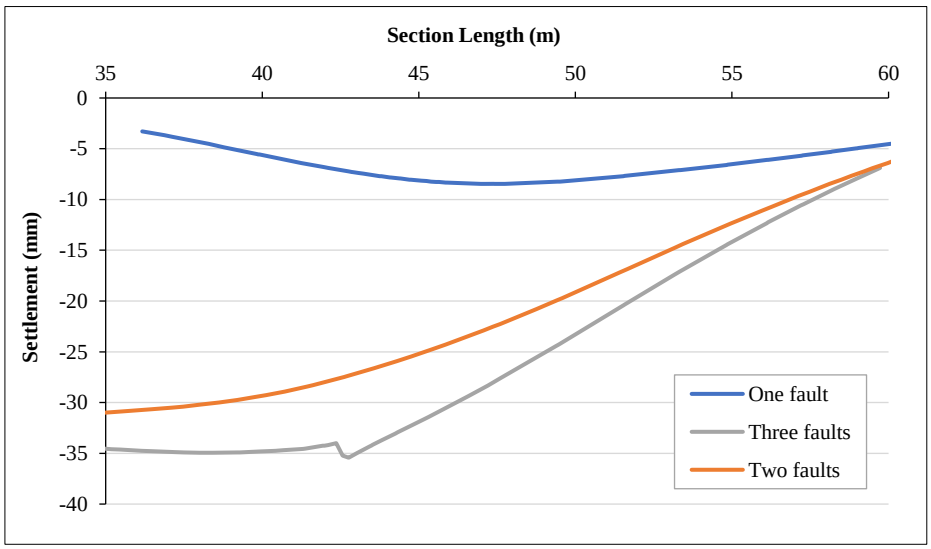

(b)

Figure 15. The settlement when the friction angel is 6 degree; (a) Along the fault, (b) Above the tunnel

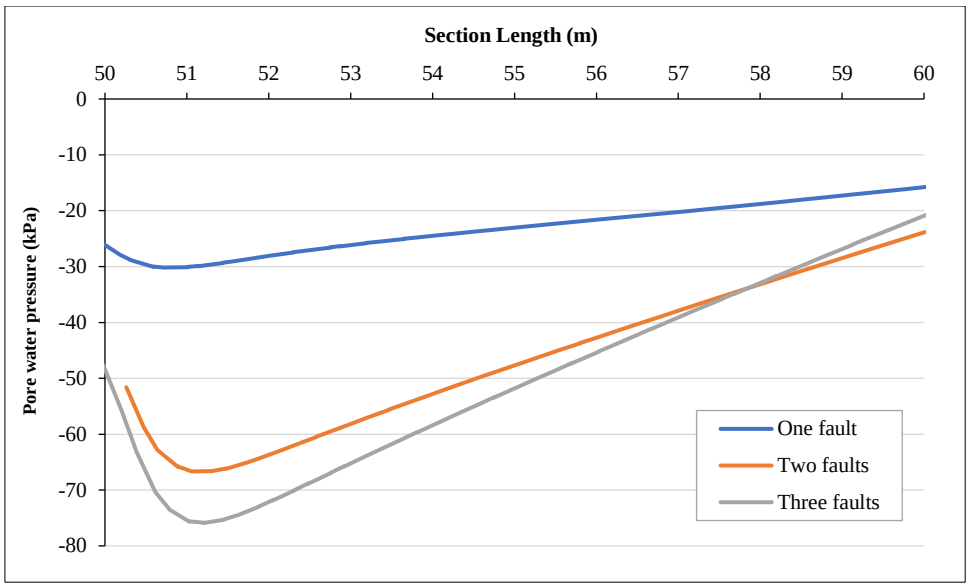

(a)

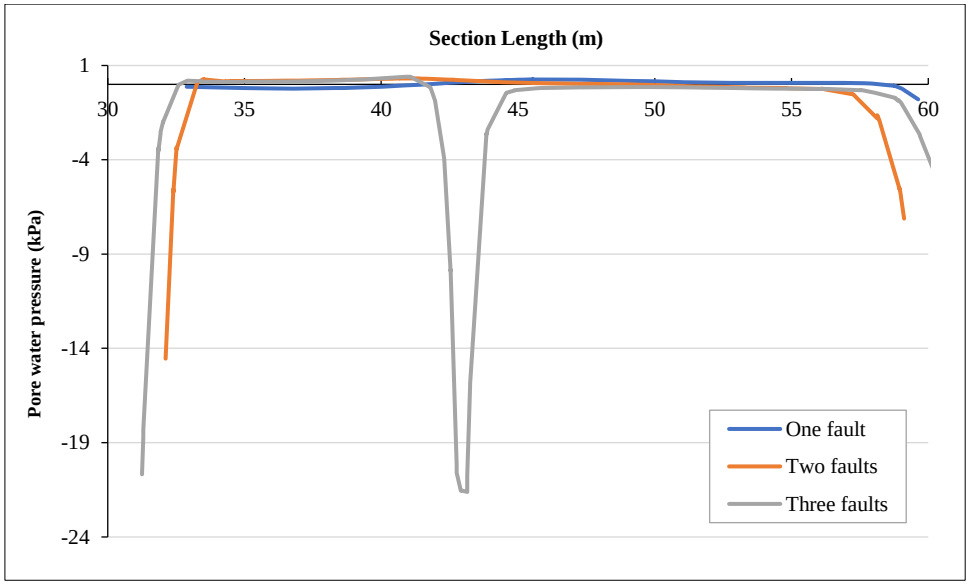

(b)

Figure 16. The pore water pressure when the friction angel is 8;(a) Along the fault, (b) Above the tunnel

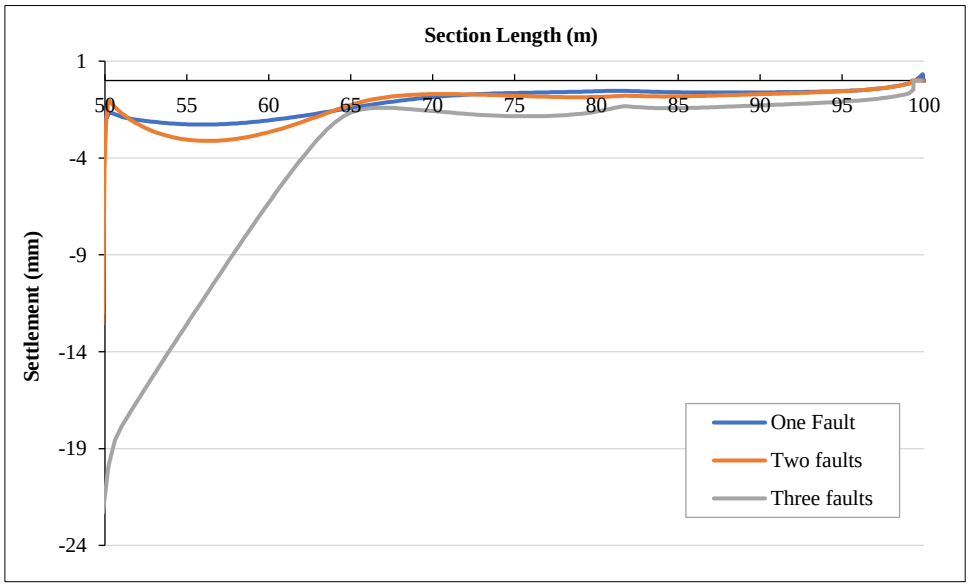

(a)

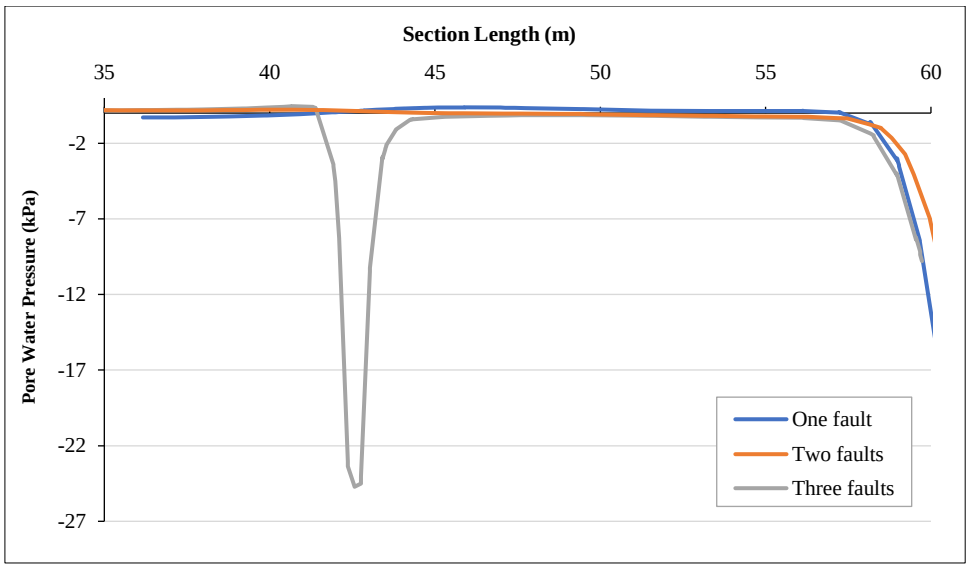

(b)

Figure 17. The pore water pressure when the friction angel is 6 degree; (a) Along the fault, (b) Above the tunnel

The observed difference in pore water pressure can be attributed primarily to the influence of the friction angle on soil shear strength, deformation characteristics, and drainage behavior. A higher friction angle (8°) corresponds to greater shear strength and increased resistance to deformation, which limits soil compressibility and reduces the dissipation pathways for pore water. Under these conditions, the presence of multiple faults acts as a barrier system that interrupts flow continuity, leading to the accumulation and concentration of pore water pressure, particularly along the fault zone. In contrast, a lower friction angle (6°) indicates weaker soil with higher deformability, allowing for greater volumetric strain and enhanced redistribution of pore water. This facilitates more efficient dissipation of excess pore pressure, resulting in significantly lower recorded values.

Additionally, the increased deformability in the lower friction angle case reduces the ability of faults to trap water pressure, further contributing to the reduced pore water pressure magnitude. However, in the section that is located above the tunnel, there is not much difference in the pore water pressure values. The negligible difference in pore water pressure above the tunnel for friction angles of 8° and 6° can be explained by the dominance of hydraulic boundary conditions and geometric effects over shear strength parameters in this region. Above the tunnel, pore water pressure is primarily governed by seepage flow, rainfall infiltration, and drainage conditions rather than by the shear strength of the soil. Since the friction angle mainly influences mechanical resistance and shear behavior, its effect on pore pressure becomes secondary in zones where fluid flow is the controlling mechanism. Moreover, the tunnel cavity acts as a stress relief and drainage boundary, promoting redistribution and partial dissipation of pore water pressure regardless of the friction angle value. As a result, both cases (8° and 6°) exhibit similar pore water pressure responses in this section. In addition, the absence of strong confinement or fault-induced trapping above the tunnel limits the accumulation of excess pore pressure, further reducing the sensitivity of this region to variations in friction angle.

Based on the foregoing analysis, it can be concluded that mechanical parameters—such as the friction angle, cohesion, and modulus of elasticity—exert a greater influence on settlement than pore water pressure. This indicates that, in the studied sections, soil strength and stiffness properties predominantly govern deformation behavior, while variations in pore water pressure have a comparatively minor effect on the overall settlement response.

The parametric results provide several practical implications for tunnel design in faulted ground under rainfall conditions. First, the number and spatial distribution of faults should be carefully identified during the site investigation stage, as increasing fault multiplicity was found to amplify settlement by creating weakened zones and preferential deformation paths. Second, the modulus of elasticity of the fault material should be treated as a key design parameter, since lower stiffness produced a more significant increase in settlement than variations in cohesion or friction angle. This indicates that deformation-based design and stiffness characterization are essential when tunnels pass through weak or fractured zones. Third, although pore water pressure was less sensitive to mechanical parameters, it remains strongly governed by rainfall infiltration, permeability, and hydraulic boundary conditions; therefore, drainage systems, waterproofing measures, and groundwater control should be incorporated into the design. Finally, the comparison between grouted and ungrouted cases indicates that pre-excavation grouting can effectively reduce deformation and enhance ground stability. Accordingly, for tunnels crossing weak fault zones in rainfall-prone areas, the design should combine detailed geological investigation, stiffness-based settlement assessment, adequate drainage control, and targeted pre-reinforcement to reduce construction risk and improve long-term tunnel performance.

4. Discussion

Based on the previously conducted parametric study, the most critical parameters were identified and selected to establish an optimal design scenario. Following this selection, grouting was implemented as a mitigation measure through injection into the three identified fault zones. Subsequently, a comparative analysis was performed between the grouted and ungrouted cases in order to evaluate the effectiveness of the grouting treatment on the system response. The results indicate that the implementation of grouting prior to excavation significantly enhances slope stability and reduces the magnitude of deformation as shown in Figure 18.

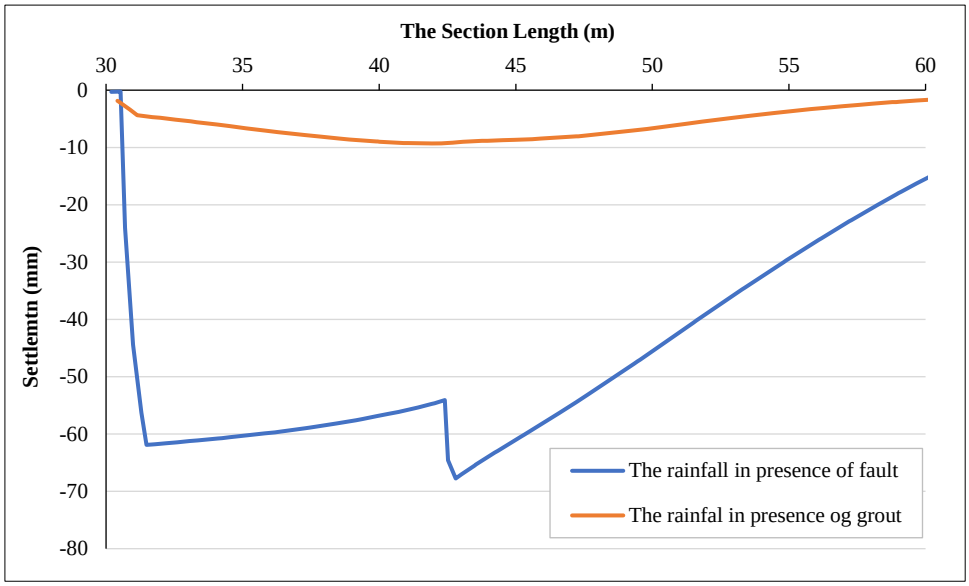

Figure 18. A comparison between the grouted and ungrouted case

5. Conclusion

This study investigated tunnel-induced settlement in faulted rock masses under rainfall conditions through an integrated approach combining analytical solutions and numerical modeling. The analytical solution, based on elastic cavity theory, was first validated against finite element simulations, demonstrating strong agreement in both trend and magnitude of settlement. A comprehensive parametric study was then conducted to examine the influence of key mechanical and geological parameters, including the number of faults, modulus of elasticity, cohesion, and internal friction angle. The results indicate that fault characteristics significantly influence deformation behavior, with increasing fault multiplicity producing higher settlements due to localized weakening and the creation of preferential deformation paths. Among the mechanical parameters considered, the modulus of elasticity emerged as the most influential factor controlling settlement, whereas variations in cohesion and friction angle produced comparatively smaller effects. Pore water pressure, in contrast, was found to be predominantly governed by hydraulic conditions, with mechanical properties exerting a secondary role. These findings highlight the critical interplay between geological discontinuities and soil-rock mechanical properties in determining tunnel-induced deformation, particularly in rainfall-affected conditions.

The study also evaluated mitigation strategies, with cement grouting implemented prior to excavation shown to substantially enhance slope stability and reduce settlement. The effectiveness of pre-reinforcement underscores the importance of integrating mitigation measures into design for faulted and rainfall-prone environments. Overall, the results demonstrate that tunnel stability is controlled by the coupled interaction of geological faults, material properties, and hydro-mechanical processes. The proposed analytical-numerical framework provides a practical tool for predicting tunnel-induced settlement, enabling engineers to optimize design parameters, anticipate deformation patterns, and implement targeted reinforcement strategies in complex geological settings. These insights contribute to improved safety, reliability, and performance of underground infrastructure in faulted rock masses subjected to variable environmental conditions.

6. Declarations

6.1. Author Contributions

Conceptualization, Z.A. and L.S.; methodology, Z.A. and L.S.; software, L.S. and Z.A.; validation, L.S., H.A., and Z.A.; formal analysis, L.S.; investigation, Z.A. and L.S.; resources, L.S., A.A., and H.A.; data curation, L.S. and Z.A.; writing—original draft preparation, Z.A. and L.S.; writing—review and editing, Z.A. and L.S.; visualization, L.S., Z.A., and A.A.; supervision, L.S. and Z.A.; project administration, Z.A. and L.S. All authors have read and agreed to the published version of the manuscript.

6.2. Data Availability Statement

The data presented in this study are available on request from the corresponding author.

6.3. Funding and Acknowledgments

The authors extend their appreciation to Prince Sattam bin Abdulaziz University for funding this research work through the project number (PSAU/2025/01/35302).

6.4. Conflicts of Interest

The authors declare no conflict of interest.

7. References

[1] Peck, B. B. (1969). Deep excavation and tunnelling in soft ground, State of the art volume. Proceedings of the 7th International Conference on Soil Mechanics and Foundation Engineering, 1969, Mexico City, Mexico.

[2] Sagaseta, C. (1987). Analysis of undrained soil deformation due to ground loss. Géotechnique, 37(3), 301–320. doi:10.1680/geot.1987.37.3.301.

[3] Verruijt, A., & Booker, J. R. (1996). Surface settlements due to deformation of a tunnel in an elastic half plane. Geotechnique, 46(4), 753–756. doi:10.1680/geot.1996.46.4.753.

[4] Loganathan, N., & Poulos, H. G. (1998). Analytical Prediction for Tunneling-Induced Ground Movements in Clays. Journal of Geotechnical and Geoenvironmental Engineering, 124(9), 846–856. doi:10.1061/(asce)1090-0241(1998)124:9(846).

[5] Guo, H., Zhang, G., Wu, Z., & Wang, J. (2025). The Control of Shield Tunnel Construction-Induced Ground Settlement Based on an Optimized Gap Parameter Theory and Three-Dimensional Finite Element Analysis. Buildings, 15(9), 1578. doi:10.3390/buildings15091578.

[6] Tang, K., Liu, D., Xie, S., Qiu, J., Lai, J., Liu, T., & Fang, Y. (2024). Analysis of loess water migration regularity and failure response of tunnel structure under rainfall environment. Bulletin of Engineering Geology and the Environment, 83(6), 251. doi:10.1007/s10064-024-03715-9.

[7] Wang, Z., Hu, M., Lai, J., Xie, S., & Cai, Y. (2023). Reliability analysis method for tunnel structural design: Brief review and relevant prospects. Structures, 55, 1894–1905. doi:10.1016/j.istruc.2023.05.104.

[8] Li, L., Wang, Q., Li, S., Huang, H., Shi, S., Wang, K., Lei, T., & Chen, D. (2014). Cause analysis of soft and hard rock tunnel collapse and information management. Polish Journal of Environmental Studies, 23(4), 1227–1233.

[9] Soga, K., Laver, R. G., & Li, Z. (2017). Long-term tunnel behaviour and ground movements after tunnelling in clayey soils. Underground Space (China), 2(3), 149–167. doi:10.1016/j.undsp.2017.08.001.

[10] Zhang, N., Zheng, Q., Elbaz, K., & Xu, Y.-S. (2020). Water Inrush Hazards in the Chaoyang Tunnel, Guizhou, China: A Preliminary Investigation. Water, 12(4), 1083. doi:10.3390/W12041083.

[11] Kim, J., Kim, C., Kim, G., Kim, I., Abbas, Q., & Lee, J. (2022). Probabilistic tunnel collapse risk evaluation model using analytical hierarchy process (AHP) and Delphi survey technique. Tunnelling and Underground Space Technology, 120, 104262. doi:10.1016/j.tust.2021.104262.

[12] Zheng, X., Zhang, L., Wu, S., & Song, K. (2021). Study on the shape of the aerator of high-head discharge tunnel with mild bottom slope. Water (Switzerland), 13(15), 2128. doi:10.3390/w13152128.

[13] Farghaly, A. A., & Kontoni, D. P. N. (2018). Train induced dynamic response of a pedestrian tunnel under a four-track surface railway for different soil water contents. Geomechanics and Engineering, 16(4), 341–353. doi:10.12989/gae.2018.16.4.341.

[14] Gattinoni, P., Consonni, M., Francani, V., Leonelli, G., & Lorenzo, C. (2019). Tunnelling in landslide areas connected to deep seated gravitational deformations: An example in Central Alps (northern Italy). Tunnelling and Underground Space Technology, 93, 103100. doi:10.1016/j.tust.2019.103100.

[15] Xue, Y., Zhang, S., Zhou, M., & Zhu, H. (2021). Novel SfM-DLT method for metro tunnel 3D reconstruction and Visualization. Underground Space (China), 6(2), 134–141. doi:10.1016/j.undsp.2020.01.002.

[16] Guo, C., Guo, Q., Zhang, T., Li, W., Zhu, H., & Yan, Z. (2022). Study on real-time heat release rate inversion for dynamic reconstruction and visualization of tunnel fire scenarios. Tunnelling and Underground Space Technology, 122, 104333. doi:10.1016/j.tust.2021.104333.

[17] Fraldi, M., & Guarracino, F. (2010). Analytical solutions for collapse mechanisms in tunnels with arbitrary cross sections. International Journal of Solids and Structures, 47(2), 216–223. doi:10.1016/j.ijsolstr.2009.09.028.

[18] Sun, W., Liang, Q., Qin, S., Yuan, Y., & Zhang, T. (2021). Evaluation of groundwater effects on tunnel engineering in loess. Bulletin of Engineering Geology and the Environment, 80(3), 1947–1962. doi:10.1007/s10064-020-02095-0.

[19] Wang, J., Lin, G., Xu, G., Wei, Y., Li, S., Tang, X., & He, C. (2022). Face stability of EPB shield tunnels in multilayered ground with soft sand lying on hard rock considering dynamic excavation process: A DEM study. Tunnelling and Underground Space Technology, 120, 104268. doi:10.1016/j.tust.2021.104268.

[20] Prendes-Gero, M. B., Lopez-Gayarre, F., Menendez-Fernandez, C., & Rodriguez-Avial Llardent, M. (2013). Forensic analysis of the failure of the foundations of a tunnel built to channel the course of a river. Engineering Failure Analysis, 32, 152–166. doi:10.1016/j.engfailanal.2013.01.004.

[21] Li, P., Zhao, Y., & Zhou, X. (2016). Displacement characteristics of high-speed railway tunnel construction in loess ground by using multi-step excavation method. Tunnelling and Underground Space Technology, 51, 41–55. doi:10.1016/j.tust.2015.10.009.

[22] Luo, Y., Chen, J., Shi, Z., Li, J., & Liu, W. (2020). Mechanical characteristics of primary support of large span loess highway tunnel: A case study in Shaanxi Province, Loess Plateau, NW China primary. Tunnelling and Underground Space Technology, 104, 103532. doi:10.1016/j.tust.2020.103532.

[23] Nie, L., Wang, C., Liu, Z., Xu, Z., Sun, X., Du, Y., & Wei, W. (2023). An integrated geological and geophysical approach to identify water-rich weathered granite areas during twin tunnels construction: A case study. Tunnelling and Underground Space Technology, 135, 105025. doi:10.1016/j.tust.2023.105025.

[24] Zhang, G. H., Xie, Z. Z., Zhang, B. W., Jiao, Y. Y., Zou, J. P., Wu, J. Q., Xiong, F., & Tang, Z. C. (2024). Sources of high-temperature water and gas inrush during tunnel excavation: A case of Bangfu tunnel in Southwest China. Journal of Rock Mechanics and Geotechnical Engineering, 16(12), 5027–5049. doi:10.1016/j.jrmge.2024.01.001.

[25] Farhadian, H., Tabrizi, D. S., Yousefi, S., Rezaei, A., & Saeidi, A. (2025). Evaluation of geological hazards along the Karaj water conveyance tunnel using multiple approaches and GIS. Results in Engineering, 26, 104758. doi:10.1016/j.rineng.2025.104758.

[26] Yao, C., He, C., Takemura, J., Feng, K., Guo, D., & Huang, X. (2021). Active length of a continuous pipe or tunnel subjected to reverse faulting. Soil Dynamics and Earthquake Engineering, 148, 106825. doi:10.1016/j.soildyn.2021.106825.

[27] Kaya, A., Karaman, K., & Bulut, F. (2017). Geotechnical investigations and remediation design for failure of tunnel portal section: A case study in northern Turkey. Journal of Mountain Science, 14(6), 1140–1160. doi:10.1007/s11629-016-4267-x.

[28] Duan, X., Hou, T. Shun, & Jiang, X. Dong. (2021). Study on stability of exit slope of Chenjiapo tunnel under extreme rainstorm conditions. Natural Hazards, 107(2), 1387–1411. doi:10.1007/s11069-021-04636-6.

[29] Zhang, Y., Sun, X., Di, S., & Cui, Z. (2025). Numerical Analysis on the Effect of Geometric Parameters of Reverse Fault on Tunnel Mechanical Response. Buildings, 15(10), 15. doi:10.3390/buildings15101704.

[30] Wu, Y., Hao, R., Zhang, T., Huang, D., & Xiong, Z. (2025). Experimental and Numerical Study on the Impact of Multi-Line TBM Tunneling in Fractured Zones on Building Deformation. Buildings, 15(18), 3322. doi:10.3390/buildings15183322.

[31] Bustamante, J., Gallardo-Sepúlveda, R., Atencio, E., & Parra, P. F. (2025). Sensitivity Analysis of the Influence of Heavy-Intensity Rain Duration on the Stability of Granular Soil Slopes Under Unsaturated Conditions. Applied Sciences (Switzerland), 15(11), 6074. doi:10.3390/app15116074.

[32] Ma, Q., Zhang, X., & Shu, H. (2025). Innovative Grouting Reinforcement Techniques for Shield Tunnels: A Case Study on Surface Settlement Mitigation. Applied Sciences (Switzerland), 15(9), 4623. doi:10.3390/app15094623.

[33] Liu, X., Suliman, L., Zhou, X., & Abd Elmageed, A. (2022). Settlement characteristics due to excavate two parallel tunnels through a fill slope. International Journal of Civil Infrastructure, 5, 95–103. doi:10.11159/ijci.2022.013.

[34] Verruijt, A. (2001). Soil mechanics. Delft University of Technology, Delft, Netherlands.

[35] Das, B. M. (2019). Advanced soil mechanics. CRC Press, London, United Kingdom. doi:10.1201/9781351215183

[36] Ghafari, M., Nahazanan, H., Md Yusoff, Z., & Nik Daud, N. N. (2020). A novel experimental study on the effects of soil and faults' properties on tunnels induced by normal and reverse faults. Applied Sciences, 10(11), 3969. doi:10.3390/app10113969.

[37] Perrone, A., Vassallo, R., Lapenna, V., & Di Maio, C. (2008). Pore water pressures and slope stability: A joint geophysical and geotechnical analysis. Journal of Geophysics and Engineering, 5(3), 323–337. doi:10.1088/1742-2132/5/3/008.